

# Sustainable heat harvesting via thermal nonlinearity

Yi Zhou<sup>1</sup>, Tianpeng Ding<sup>2</sup>, Guoqiang Xu<sup>1</sup>, Shuihua Yang<sup>1</sup>, Cheng-Wei Qiu<sup>1,3</sup>, Jiaqing He<sup>4,5</sup>✉ & Ghim Wei Ho<sup>1,6</sup>✉

## Abstract

Converting the pervasive low-grade environmental waste heat of approximately 200 EJ globally per year (equivalent to 27 Gt of CO<sub>2</sub> emission) into electricity promises energy sustainability and would contribute to carbon neutrality. Heat harvesting technologies capture this waste heat through thermodynamic heat engines across various working media. Conventional heat harvesting approaches have primarily focused on limited incremental improvements in thermophysical output. However, advances in thermal nonlinearity and material anisotropy offer substantial gains but are often overlooked. In this Perspective, we delve into the role of intrinsic thermal nonlinearity with multiscale physical understanding to transform heat or thermal energy harvesting technologies from linear to nonlinear processes.

## Sections

Introduction

Fundamentals and benchmarks of nonlinear heat harvesting

Multiscale manipulations of nonlinear heat harvesting

Outlook

<sup>1</sup>Department of Electrical and Computer Engineering, National University of Singapore, Singapore, Singapore.

<sup>2</sup>School of Physics and State Key Laboratory of Electronic Thin Film and Integrated Devices, University of Electronic Science and Technology of China, Chengdu, China.

<sup>3</sup>Nanotech Energy and Environment Platform, National University of Singapore Suzhou Research Institute, Suzhou, China.

<sup>4</sup>Shenzhen Key Laboratory of Thermoelectric Materials, Department of Physics, Southern University of Science and Technology, Shenzhen, China.

<sup>5</sup>Guangdong Provincial Key Laboratory of Advanced Thermoelectric Materials and Device Physics, Southern University of Science and Technology, Shenzhen, China.

<sup>6</sup>Department of Materials Science and Engineering, National University of Singapore, Singapore, Singapore.

✉ e-mail: [hejq@sustech.edu.cn](mailto:hejq@sustech.edu.cn); [elehgw@nus.edu.sg](mailto:elehgw@nus.edu.sg)

[hejq@sustech.edu.cn](mailto:hejq@sustech.edu.cn)

## Introduction

In the energy transition from centralized fossil fuels to renewable and sustainable alternatives that target the United Nations Sustainable Development Goals (UN SDGs), there exists an important role for harvesting disordered, distributed and decentralized waste heat from the environment to produce electricity<sup>1–3</sup>. Heat dissipation into the environment is governed by the second law of thermodynamics, which states that the total entropy ( $s$ ) of an isolated system can never decrease over time (that is,  $\Delta s > 0$ ). In other words, in thermodynamic processes, the irreversibility of the Carnot heat engine (that is, the relative Carnot efficiency  $\eta_r < 1$ ) results in inevitable heat dissipation (and, thus, carbon emission). Therefore, harvesting untapped, invisible and all-present waste heat from the environment as cost-effectively and sustainably as plastic recycling has become an emerging focus not only in fundamental physics but also in the effort to meet the UN's climate targets. Heat harvesting (or thermal energy harvesting) technology is an application-driven fundamental research field that is rooted in interdisciplinarity across physics, materials science, chemistry, engineering and sustainability. Heat harvesting materials aim to convert thermal potential differences into electrostatic or electrochemical potentials (voltage) through thermodynamic cycles using various working media, such as electrons, ions, molecules, phonons, magnons or polaritons. Despite the ever-growing efforts made by academia, industry and policymakers over the past century, along with notable achievements in thermoelectrics and pyroelectrics, heat harvesting in a more sustainable way still faces several challenges. These include, but are not limited to, the need for an in-depth understanding of the physical transport of working media in the thermodynamic process at multiple scales, the development of more efficient and streamlined synthesis of heat harvesting materials, the design of effective and simplified device configurations, and the establishment of comprehensive evaluation metrics for techno-socioeconomics.

Traditionally, heat harvesting efforts have been focused on improving performance metrics or figures of merit (FOM) of materials at given boundary conditions (for example, thermodynamic cycle across low ( $T_L$ ) and high ( $T_H$ ) temperatures) in a linear manner. Examples include the following: increasing the Seebeck coefficient ( $S$ ) or thermoelectric figure of merit ( $ZT$ ) to maximize the electrical power density ( $P_D \propto S^2$ ) or power conversion efficiency ( $\eta \propto \frac{\sqrt{1+ZT}-1}{\sqrt{1+ZT}+T_L/T_H}$ ) (refs. 4–6); enhancing the change in electric polarization ( $P$ ) to boost the pyroelectric coefficient ( $p_{\text{pyro}}$ ) and current output ( $I \propto p_{\text{pyro}}, P_{\text{pyro}} = \partial P / \partial T$ ) (refs. 7–9); and lowering the water vapourization enthalpy ( $\Delta H_{\text{vapour}}$ ) to raise the evaporation rate ( $m_{\text{evp}}$ ) (refs. 10,11). However, the overall heat harvesting capability is not solely governed by these performance metrics or FOMs but hinges on the thermal nonlinearity of materials associated with spatial and temporal heat transport across multiple scales.

One of the famous implications of nonlinearity is the so-called brachistochrone problem, initially posed by Bernoulli over three centuries ago. The problem is to find the trajectory that minimizes the time it takes for a bead to slide from an upper point to a lower point on a plane, under the sole influence of gravity (without friction). Mathematical derivation reveals that a cycloid, not a linear path, yields the shortest travel time when considering only gravity (Fig. 1a). The physics behind the cycloid curve is its ability to strike a balance between maximizing speed while minimizing travel distance. The brachistochrone curve with fastest descent for a movable object moving because of its own weight (force) has been successfully applied to mechanical energy harvesting on non-flat surfaces<sup>12,13</sup>.

Analogously, when the temperature dependence of FOM of a heat harvesting method (given as a function  $f(T) \propto T^m$ , where  $T$  is the temperature and  $m$  is the scaling exponent) shifts from linearity ( $m = 1$ ) to nonlinearity ( $m \neq 1$ ), the normalized output can be substantially greater than ( $m > 1$ ) that of conventional incremental results (Fig. 1b), owing to the increase in positive temperature differentials ( $\partial^2 / \partial T^2 > 0$ ) at consistent thermal inputs. From the viewpoint of thermodynamic energy conversion, this phenomenon of temperature nonlinearity has applications across the material, device and system levels in various heat harvesting technologies such as thermal desalination<sup>14,15</sup>, pyroelectrics<sup>16–19</sup>, thermoelectrics<sup>20,21</sup>, thermogalvanics<sup>22,23</sup>, thermomagnetism<sup>24,25</sup> and thermochromism<sup>26,27</sup>. More importantly, the performance metrics exhibit nonlinear temperature dependence and correlations with material anisotropy. This implies that the FOM could be dynamically modulated through multiscale nonlinear thermal manipulation across in-plane and out-of-plane directions in the temporal ( $\partial T / \partial t$ ) and spatial ( $\partial T / \partial x$ ) domains (where  $t$  and  $x$  refer to time and coordinate, respectively), in conjunction with tailoring material properties. Unfortunately, the fundamental understanding, current challenges, and opportunities of the abovementioned thermal nonlinearity in heat harvesting have not been well summarized and discussed to date.

In this Perspective, we begin by discussing the fundamental physics of heat transfer at the macroscale and microscale. We elucidate the mechanism by which thermal nonlinearity (specified as temperature nonlinearity, nonlinear temperature dependence or distribution) in tandem with governing equations and  $T$ -dependent FOMs contribute to heat harvesting technologies towards desirable thermodynamic energy conversion. Then, the strategies and benchmarks in thermoelectricity, pyroelectricity and thermal desalination technologies using nonlinear processes are highlighted. We specifically emphasize the significance and effectiveness of thermal nonlinearity for sustainable heat harvesting from atomic and nanoscale, microscale, mesoscale and macroscale thermal transport in thermoelectrics and pyroelectrics. We also showcase the potential of thermal nonlinearity to revolutionize the way heat is harvested with higher energy efficiency and lower carbon footprint to meet the UN SDGs. Finally, we outline the challenges and opportunities in nonlinear heat harvesting and offer insights into future prospects.

## Fundamentals and benchmarks of nonlinear heat harvesting

### Fundamental physics of thermal nonlinearity

From a macroscopic heat transfer viewpoint, the temperature field of an object ( $T(x, y, z, t)$  in 3D Cartesian coordinates) is normally governed by heat conduction, heat radiation and heat convection (Box 1). The mathematical formulation of heat transfer across an object, whether in a steady or transient state, actually involves deriving the analytical or numerical solution of  $T(x, y, z, t)$  from partial differential equations of heat transport associated with given initial and boundary conditions

$$\rho C_p \frac{\partial T}{\partial t} = \frac{\partial}{\partial x} \left( \kappa \frac{\partial T}{\partial x} \right) + \frac{\partial}{\partial y} \left( \kappa \frac{\partial T}{\partial y} \right) + \frac{\partial}{\partial z} \left( \kappa \frac{\partial T}{\partial z} \right) + Q_{\text{in}} \quad (1)$$

where  $\rho$  is density,  $C_p$  is specific heat capacity,  $\kappa$  is thermal conductivity tensor with inclusion of electronic ( $\kappa_e$ ) and lattice vibration ( $\kappa_l$ ) contribution, and  $Q_{\text{in}}$  is the internal volumetric heat source (such as the Peltier effect); all these parameters are variables with respect to  $T$ , the coordinates ( $x, y, z$ ), and  $t$ . In general, boundary conditions are

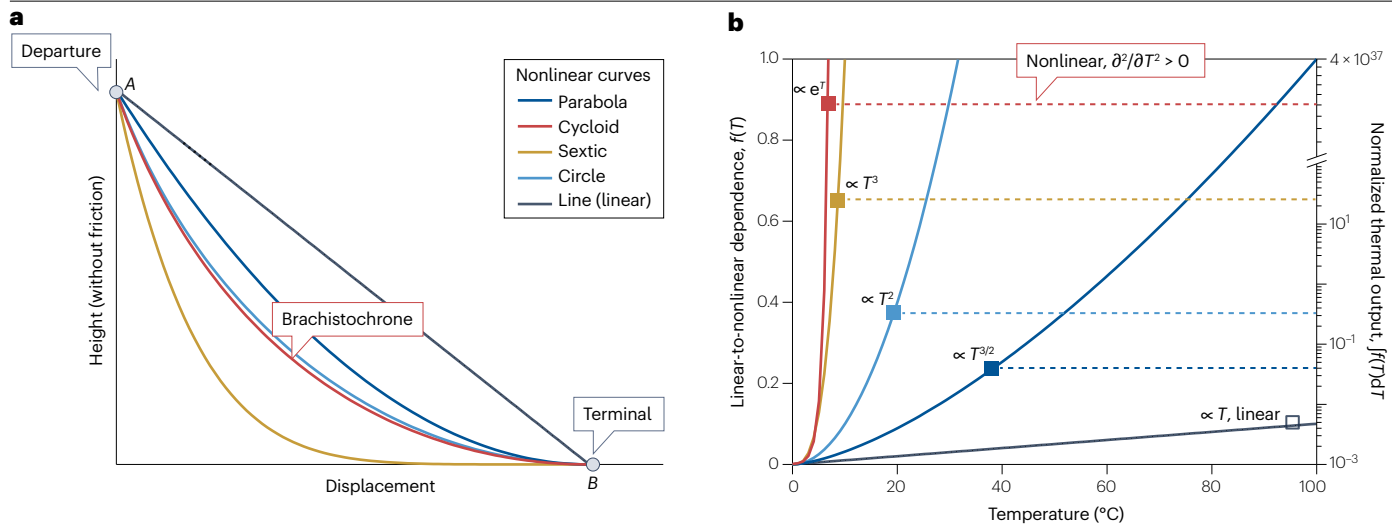


**Fig. 1 | Nonlinearity is better than linearity.** **a**, Brachistochrone or ‘shortest time’ problem. The shortest-time path for a frictionless bead subject to gravity to slide from the departure to the terminal point is given by the cycloid and not a linear path. **b**, Linear-to-nonlinear temperature dependence of figure of merit (left axis) and normalized thermal output (right axis).  $f(T)$  refers to the

temperature dependence of figures of merit. The output of  $f(T)$  is the dependent variable versus the temperature and is normalized to 1. The normalized thermal output is calculated as the integral of  $f(T)$  from the initial temperature to  $100^{\circ}\text{C}$  (that is,  $\int f(T)dT$ ), according to the general thermodynamic process of heat harvesting technologies.

classified into three categories, namely type I (Dirichlet) with a fixed temperature ( $T_H$  and  $T_L$ ), type II (Neumann) with a fixed heat flux of  $-\kappa\nabla T$ , and type III (Robin) with known  $h_{\text{conv}}$  and  $T_f$  (that is,  $h_{\text{conv}}(T - T_f)$ , where  $T_f$  is fluid temperature). Conventionally,  $\kappa$  is scalar and invariable in isotropic materials, so  $T(x, y, z, t)$  is rewritten as

$$\frac{\partial T}{\partial t} = a\nabla^2 T + \frac{Q_{\text{in}}}{\rho C_p}, \quad (2)$$

where  $a$  is thermal diffusivity. In the steady state, that is,  $\partial T/\partial t = 0$ , the governing equation of  $T(x, y, z)$  is given as  $\nabla^2 T + Q_{\text{in}}/\kappa = 0$ , which is the Poisson equation. Meanwhile, in the absence of  $Q_{\text{in}}$ , the transient  $T(x, y, z, t)$  is governed by  $\partial T/\partial t = a\nabla^2 T$ . Consequently, at low or room temperature and invariable thermal properties, equation (2) offers a straightforward solution to numerically visualize  $T(x, y, z, t)$  both in the steady ( $\partial T/\partial t = 0$ ) and transient ( $\partial T/\partial t \neq 0$ ) states for spatial and temporal heat harvesting. For instance, in terms of body heat harvesting, the attainable  $\Delta T$  is around  $5^{\circ}\text{C}$ ; therefore,  $S$  and  $\kappa$  of thermoelectrics are nearly constant when estimating  $P_D$ . However, with the inclusion of  $T$ -dependent phase changes, the  $T(x, y, z, t)$  is modelled by the energy equation<sup>28</sup>

$$\rho C_p \frac{\partial T}{\partial t} + \rho C_p v \nabla T = \nabla(\kappa \nabla T), \quad (3)$$

where  $v$  is dynamic viscosity,  $C_p$  is specific heat capacity with the inclusion of latent heat of phase change, and  $\rho$ ,  $v$ ,  $C_p$  and  $\kappa$  are  $T$ -dependent variables.

In microscale and nanoscale heat transfer (Box 1), the interaction time ( $10^{-9}$ – $10^{-12}$  s) and length scale ( $10^{-9}$ – $10^{-7}$  m) of heat transport may approach the intrinsic physical characteristics (such as relaxation time  $\tau$  and mean free path  $\Lambda$ ) of carriers. Consequently,  $T(x, y, z, t)$  is governed by  $\tau$  and  $\Lambda$ . This regime is known as non-Fourier heat transfer. Two

models are widely used to capture the wave-like behaviour of nanoscale heat transport<sup>29–31</sup>: the Cattaneo–Vernotte equation with the inclusion of thermal inertia effects, and the dual-phase-lag model. More explicitly, the wave-like lattice vibrations are modelled as quantized energy carriers (phonons). According to the Boltzmann transport equation in the relaxation time approximation and the Debye model<sup>32,33</sup>, phonon dispersion (frequency versus wave vector,  $\omega$ - $q_{\text{ph}}$ ) can be manipulated via both externally applied fields and  $\tau$ - $T$  correlations under elastic and inelastic phonon scatterings (such as phonon–phonon scattering, phonon–electron scattering and phonon–defect scattering). In particular, at low temperatures ( $T \ll \theta_D$ , where  $\theta_D$  is the Debye temperature), phonon–defect scattering dominates the heat transport and  $\kappa_L \propto T^3$ ; at intermediate temperatures ( $T \approx \theta_D/3$ ), both normal (N) and Umklapp (U) scattering processes contribute and  $\kappa_L$  peaks at a certain value before it decreases as the U scattering process becomes dominant; at high temperatures ( $T > \theta_D/3$ ), U scattering process dominates the heat transport and  $\kappa_L \propto T^{-1}$ . An in-depth understanding of the nonlinear  $T$ -dependent  $\omega$  in conjunction with the manipulation of  $\tau$  and  $\Lambda$  not only enables the engineering of  $\omega$ - $q_{\text{ph}}$  and the achievement of ultrahigh or ultralow  $\kappa_L$ , but also contributes to bridging thermal nonlinearity with FOMs targeting efficient heat harvesting.

## Thermal nonlinearity in heat harvesting

The nonlinearity of  $T(x, y, z, t)$  can be caused by steady or transient heat flux across the object; such a temperature profile is pivotal for modulating the intrinsic temperature nonlinearity of thermophysical metrics or FOMs. In the context of the thermodynamic process of an ideal Carnot engine, the working media (for example, electrons, ions, molecules, phonons, magnons or polaritons) dominate the heat and mass transport associated with thermal nonlinearity in thermophysical outputs. To showcase the significance of how nonlinear  $T$ -dependent thermophysical output contributes to emerging heat harvesting technologies under steady or transient conditions, we interpret physical

## Box 1 | Fundamental physics of thermal nonlinearity in heat harvesting

### Macroscopic heat transfer

**Heat conduction** (see the figure, part **a**). The conductive heat flux ( $\mathbf{q}_{\text{cond}}$ ) across an object (with thermal conductivity tensor of  $\kappa$ ) under a temperature gradient ( $\nabla T$ ) is given by Fourier's law  $\mathbf{q}_{\text{cond}} = -\kappa \nabla T$ . In general,  $\kappa$  is governed by both charge carriers and lattice vibration (quantized thermal carriers, that is, phonons). The latter is also specified as lattice thermal conductivity ( $\kappa_L$ ); it dominates heat transfer in non-metallic materials and is given as  $\kappa_L = C_V v_g \tau$ , where  $C_V$  is the specific heat,  $v_g$  is the group velocity and  $\tau$  is the relaxation time. Conventionally,  $\kappa_L$  is uniform (a scalar) and proportional to  $T$  in isotropic materials and ranges from  $10^{-2} \text{ W m}^{-1} \text{ K}^{-1}$  (air) to  $10^2 \text{ W m}^{-1} \text{ K}^{-1}$  (silver).

The mechanical exfoliation of van der Waals non-centrosymmetric crystals at the nanoscale, alongside porosity tailoring and graded composition at micro and mesoscales, has been used to produce a nonlinear  $\kappa$  with respect to  $T$ ,  $x$  and  $t$  variation.  $\kappa(T, x, t)$  can be predicted theoretically using effective medium theory<sup>148</sup>.

**Heat radiation** (see the figure, part **b**). The interaction phenomena between photons and the surface of objects include reflection, absorption and transmission. According to Kirchhoff's law, emissivity ( $\epsilon$ ) equals the absorptivity of an arbitrary body that emits and absorbs thermal radiation in thermodynamic equilibrium. Heat radiation or thermal electromagnetic radiation ( $\mathbf{q}_{\text{rad}}$ ) enables the transformation of energies both in amounts and forms between the heated surface and environment, which is normally given by the Stefan–Boltzmann law with a heat radiation vector direction of  $\mathbf{n}_{\text{rad}}$

$$-\mathbf{n}_{\text{rad}} \cdot \mathbf{q}_{\text{rad}} = \epsilon \sigma_{\text{SB}} (T_{\text{amb}}^4 - T^4),$$

where  $\sigma_{\text{SB}}$  is the Stefan–Boltzmann constant. The nonlinear characteristics of  $\epsilon$  with respect to wavelength, temperature and radiation angle enable the manipulation of thermal radiation towards

desirable energy harvesting and management. Moreover, the balance between absorptivity and emissivity can be broken in non-reciprocal systems and beyond Kirchhoff's law<sup>149,150</sup>.

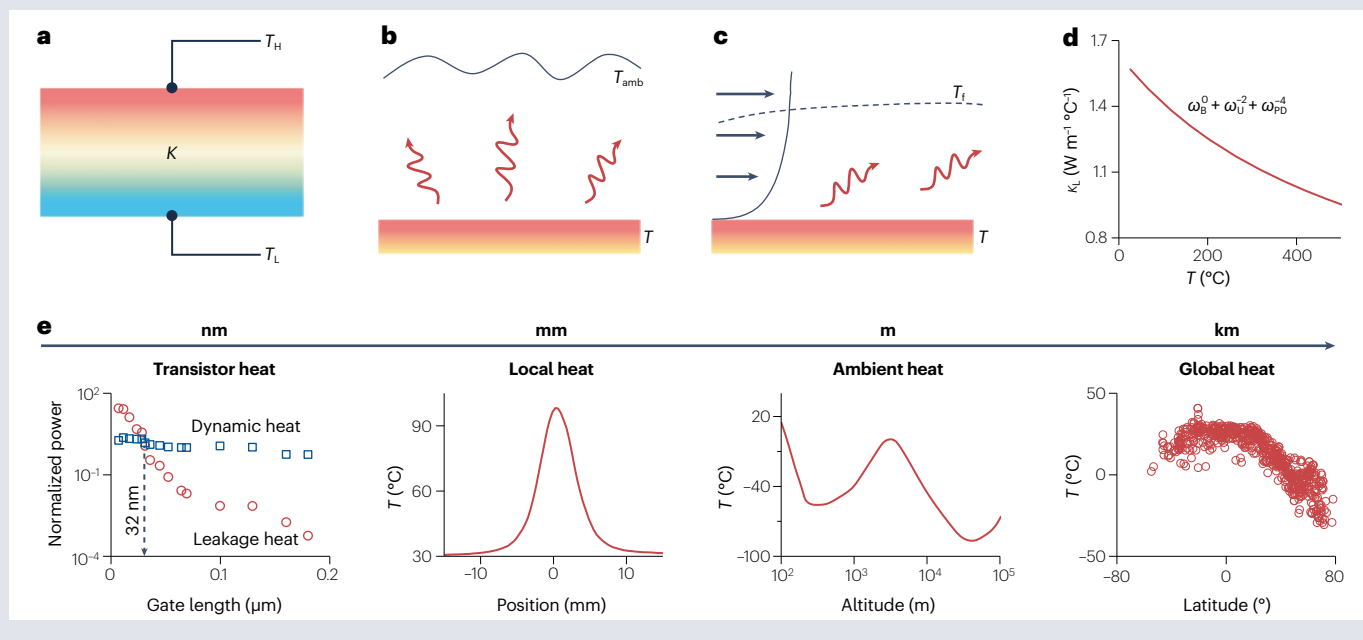
**Heat convection** (see the figure, part **c**). Heat convection is an analogue of mass transfer convection and describes how heat travels over a surface from one place to another owing to movable fluid flow. At a flat surface, the convective heat flux ( $\mathbf{q}_{\text{conv}}$ ) is described by Newton's law of cooling  $-\mathbf{n}_{\text{conv}} \cdot \mathbf{q}_{\text{conv}} = h_{\text{conv}} (T_f - T)$ , where  $h_{\text{conv}}$  is the heat transfer coefficient,  $T_f$  is the fluid temperature, and  $\mathbf{n}_{\text{conv}}$  is the heat convection vector direction. Active manipulation of  $h_{\text{conv}}$  such as the physical property or situation, enables substantial change in the spatial and temporal temperature profile of the thermal object.

### Microscopic temperature nonlinearity of lattice thermal conductivity

In accordance with the Boltzmann transport equation in the presence of a temperature gradient alongside the Planck distribution function and relaxation time, the  $\kappa_L$  can be phenomenologically fitted by the Debye–Callaway model<sup>32,33</sup> (see the figure, part **d**) and written as

$$\kappa_L = \frac{k_B}{2\pi^2 v_s} \left( \frac{k_B T}{\hbar} \right)^3 \int_0^{\theta_D} \tau_{\text{tot}} \frac{z^4 e^z}{(e^z - 1)^2} dz,$$

where  $k_B$  is the Boltzmann constant,  $\hbar$  is the reduced Planck constant,  $v_s$  is the average sound speed,  $\theta_D$  is the Debye temperature,  $z$  is the reduced phonon frequency ( $z = \hbar \omega / k_B T$ ), and  $\tau_{\text{tot}}$  is the total relaxation time and is of  $z$  dependence. Normally,  $\tau_{\text{tot}}$  is given by Matthiessen's rule in the consideration of Umklapp scattering process, point defects scattering, boundaries scattering, dislocation scattering and/or electron–phonon scattering.



(continued from previous page)

## Multiscopic temperature nonlinearity of environmental thermal devices, systems and sources

The temperature field of a thermal object (such as a heated device or system) in a steady or transient state is typically governed simultaneously by heat conduction, radiation and convection. Interestingly, temperature nonlinearity intrinsically exists in the device or system with a spatial length nanometres to kilometres; see the figure, part **e** that necessitates the active manipulation of heat

transfer for energy harvesting and management. For instance, the heat dissipation of transistors increases dramatically when the gate length approaches the nanoscale<sup>151,152</sup>, the spatial temperature profile of heated devices follows a Gauss distribution under constant heat flux<sup>16</sup>, and the ambient and global heat vary nonlinearly versus the altitude and latitude<sup>153</sup>. These common but unexplored phenomena of thermal nonlinearity in ambient sources could revolutionize heat harvesting.

insights and governing equations in accordance with equations (2) and (3), as shown in Table 1 and Fig. 2a.

Fundamentally, one of the major focuses in heat harvesting is how to manipulate and align  $T(x,y,z,t)$  with FOMs at given initial and boundary conditions with respect to externally applied multiphysical fields. From a microscopic viewpoint, changes in  $\omega$ - $q_{\text{ph}}$  or  $\kappa_{\text{L}}$  necessitate a physical interpretation of interaction phenomena and transport characteristics of energy carriers. For instance, particularly in metals, the electronic excitations modulated by coupling to lattice vibrations during electron–phonon scattering substantially influence the thermodynamic properties of the metal (such as  $\kappa$  and electrical conductivity  $\sigma$ ). In addition, the Wiedemann–Franz law states that the ratio of electronic contribution ( $\kappa_{\text{e}}$ ) of  $\kappa$  to  $\sigma$  varies linearly with  $T$ , that is,  $\kappa_{\text{e}}/\sigma = LT$ , where  $L$  is known as Lorenz number. As a result, electron–phonon decoupling is needed to reduce  $\kappa_{\text{L}}$  towards a high FOM because  $ZT \propto 1/\kappa_{\text{L}}$  and  $\kappa_{\text{e}}$  is less adjustable, especially in typical thermoelectric materials (degenerate semiconductors) with a small bandgap ( $E_{\text{g}}$ ). By contrast, the modulation of  $\kappa_{\text{L}}$  in dielectrics or insulators with a large  $E_{\text{g}}$  (for instance, clamped-lattice polar materials) tends to be the ‘opposite’, because the variation of  $\mathbf{P}_{\text{s}}$  (spontaneous polarization vector) or electric dipole moment is predominated by the harmonic vibration of ions relative to phonon propagation<sup>16,34</sup>. In another example, concerning solar-thermal desalination, temperature nonlinearity at a molecular level has been studied with the aim of increasing  $m_{\text{evp}}$  through several means: the reduction in  $\Delta H_{\text{vapour}}$  owing to modified bonding interactions between intermediate water molecules and polymer networks<sup>10</sup>; the exponential correlation of the vapour saturation pressure  $p_{\text{vapour}}(T)$  governed by the Antoine equation<sup>15</sup>; and the photo-molecular effect<sup>11</sup>.

Conversely, from a viewpoint of macroscale observations, the thermophysical properties typically show a sharp variation before reaching a critical temperature (such as the Curie temperature,  $T_{\text{Curie}}$ ) when phase transition (or phase change) materials are used in heat harvesting (Fig. 2a). For example, the unusual behaviours of  $S(T)$  and  $C_{\text{p}}(T)$  in liquid-like thermoelectrics owing to a structural phase transition as the temperature is increased from low to high<sup>35,36</sup>, the giant  $p_{\text{pyro}}(T)$  change in polar dielectrics attributed to the ferroelectric to paraelectric (FE–PE) phase transition<sup>16,37</sup>, and the large magnetic entropy variation in thermomagnetic alloys during the transition between ferromagnetic and paramagnetic states (FM–PM transition)<sup>25</sup>. Moreover, the nonlinear temperature dependence of  $p_{\text{vapour}}(T)$ ,  $S(T)$ ,  $p_{\text{pyro}}(T)$  and Carnot efficiency ( $\eta_{\text{Carnot}}$ ) proves that colossal thermophysical output can be realized at elevated temperatures<sup>38,39</sup>. Accordingly, making use of temperature-dependent energy harvesting capabilities beyond traditional linear characteristics requires that waste heat be upgraded from low grade (around room temperature) to high grade (for example, close to but just below  $T_{\text{Curie}}$ ).

## Benchmarks of nonlinear heat harvesting

Advances in the study of thermal nonlinearities have led to promising developments in electricity and water production through solar heat harvesting over the past decade (Fig. 2b). In particular, under consistent input heat flux, transverse pyroelectricity is verified to offer a high  $P_{\text{D}}$  ( $\approx 38 \text{ mW m}^{-2}$ ), two orders of magnitude greater than that of conventional linear methods ( $\approx 0.1 \text{ mW m}^{-2}$ ) (refs. 16,40–46). This unexpected finding is mainly ascribed to the synergistic increase of  $\partial T/\partial t$  and  $p_{\text{pyro}}(T)$  under in-plane heat generation and propagation decoupling. Similarly, the topological anisotropy of thermoelectrics has transformed the solar heat harvesting process by incorporating a non-unity configuration (for example, dissimilar geometry of p-type and n-type legs) and spectral selectivity (for example, passive solar heating and/or radiative cooling). Doing so results in an increase of the effective  $\Delta T$  across the thermoelectric legs, targeting a  $P_{\text{D}}$  increase of three orders of magnitude, far greater than that of conventional unity structures<sup>47–52</sup>. Apart from heat-to-electricity generation, thermal nonlinearity has found applications in solar vapourization of thermal desalination via thermal and/or optical concentrations, leading to an improvement of two to three orders of magnitude in  $m_{\text{evp}}$  (refs. 15,53–55). Fundamentally, these extremely high performances are attributed to the nonlinear temperature dependence of thermophysical properties and material anisotropy (Fig. 2a). This facile yet overlooked phenomenon in conventional linear systems opens new avenues for highly efficient and sustainable heat harvesting, as demonstrated through multiscale thermal manipulations.

## Multiscale manipulations of nonlinear heat harvesting

The heat harvesting capability (for example,  $P_{\text{D}}$  or  $\eta$ ) with respect to a given  $T(x,y,z,t)$  is fundamentally determined by the lattice heat transport ( $\kappa$ ) in conjunction with thermophysical metrics or FOMs (such as  $ZT$ ,  $S(T)$ ,  $p_{\text{pyro}}(T)$ ). In crystalline solids, such as thermoelectric semiconductors and polar dielectrics, heat transport can be modelled as the propagation and scattering of phonons across the lattice. Normally,  $\kappa$  is composed of spectral volumetric specific heat ( $C_{\text{v}}(\omega)$ ), group velocity ( $v_{\text{g}}(\omega)$ ) and relaxation time ( $\tau(\omega)$ ), and given by integration of phonon spectra. Concerning the Bose–Einstein distribution  $f$  and the phonon density of states ( $N(\omega)$ ), here  $C_{\text{v}}(\omega)$  can be written as  $\hbar\omega N(\omega) \frac{\partial f}{\partial T}$ , and  $\Lambda(\omega) = v_{\text{g}}(\omega)\tau(\omega)$  (ref. 56). In the domain of thermoelectrics, the phenomenological description of  $\kappa_{\text{L}}$  is fitted using the Debye–Callaway model<sup>32,33</sup>. A simple way to approach the theoretical limit of  $\kappa_{\text{L}}$  is to tailor  $\tau(\omega)$  according to various scattering processes (Box 1). By contrast, for pyroelectrics, in accordance with the Born–Szigeti quantum theory<sup>19,57</sup>, the primary  $p_{\text{pyro}}(T)$  is attributed to the harmonic variation of ions (known as electron–phonon renormalization) and anharmonic potential (known as ridge-ion displacement). Consequently, in thermal

**Table 1 | Summary of nonlinear heat harvesting**

Technologies	Governing equations	Notes	Nonlinearity
Thermal desalination <sup>a</sup>	Discretization of the continuity, momentum and energy equations in consideration of air, liquid and vapour phases; the mixture phase of vapour and liquid is modelled using Lee model <sup>137,138</sup> : $\frac{\partial \rho_m}{\partial t} + \nabla \cdot (\rho_m \mathbf{u}_m) = 0,$ $\frac{\partial}{\partial t} \sum_{k=1}^m (\beta_k \rho_k E_k) + \nabla \cdot \sum_{k=1}^m [\beta_k \mathbf{u}_k (\rho_k E_k + p)] = \nabla \cdot (K_{\text{eff}} \nabla T) + Q_E,$ $\frac{\partial (\beta_v \rho_v)}{\partial t} + \nabla \cdot (\beta_v \rho_v \mathbf{u}_m) = m_{\text{evp}}$	$\rho_m$ is the density of the mixture and is given as $\rho_m = \sum_{k=1}^m \beta_k \rho_k$ , where $k$ is the phase; $\mathbf{u}_m$ is the mass-averaged velocity; $\beta_v$ is vapour volume fraction; $\rho_v$ is the vapour density; $\mathbf{u}_v$ is the velocity of vapour; $m_{\text{evp}}$ is evaporation rate; $E_k$ equals $\Delta H_{\text{vapour}}(T)$ for incompressible phase; $K_{\text{eff}}$ is the volumetric thermal conductivity of mixture	Vapour saturation pressure $p_{\text{vapour}}(T) \propto e^1$ according to Antoine equation; nonlinear $T$ -dependent of vaporization enthalpy $\Delta H_{\text{vapour}}(T)$ according to Clausius–Clapeyron equation, interbond-dependent $\Delta H_{\text{vapour}}$ ; manipulative $h_{\text{conv}}$
Pyroelectric <sup>b</sup>	Heat transfer at transient state, including heat conduction, radiation, convection and electrostatic equations <sup>16,139</sup> : $\rho C_p \frac{\partial T}{\partial t} + \rho C_p \mathbf{u} \cdot \nabla T + \nabla \cdot (-\kappa \nabla T) = Q,$ $\nabla \cdot \mathbf{D} = \rho_{\text{ex}},$ $\mathbf{E} = -\nabla V,$ $\mathbf{D} = \epsilon_0 \mathbf{E} + \mathbf{P}$	Volumetric or space charge density $\rho_c$ is of nonlinear $T$ -dependence; $\mathbf{D}$ is electric displacement; $\mathbf{E}$ is electric field; the total polarization ( $\mathbf{P}$ ) is given as $\mathbf{P} = \mathbf{P}_s + \mathbf{P}_E$ , where $\mathbf{P}_s$ and $\mathbf{P}_E$ are spontaneous and electric field-driven polarization, respectively	Pyroelectric coefficient $p_{\text{pyro}} = \partial P / \partial T$ and $p_{\text{pyro}} \propto T^3$ , $P$ is the element of polarization; pyroelectric current $I = p_{\text{pyro}} A \partial T / \partial t$ ; FOM = $p_{\text{pyro}} / (\epsilon C_p)$ ; $\mathbf{P}_s(T)$ , $\mathbf{P}_E(T)$ , $\epsilon(T)$ and $C_p(T)$ are $T$ -dependent; manipulative $\epsilon$ and $h_{\text{conv}}$ ; anisotropic $\mathbf{P}_s(T)$ and $\mathbf{P}_E(T)$
Thermoelectric <sup>c</sup>	Heat transfer and current conservation equations alongside Seebeck effect, Peltier effect and Thomson effect <sup>63</sup> : $\rho C_p \mathbf{u} \cdot \nabla T + \nabla \cdot \mathbf{q} = JE,$ $\mathbf{E} = -\nabla V,$ $\mathbf{q} = -\kappa \nabla T + ST\mathbf{J},$ $\mathbf{J} = -\sigma \nabla V - \sigma S \nabla T$	$\mathbf{J}$ is electric current density, $V$ is voltage; $\mathbf{S}$ , $\kappa$ and $\sigma$ are Seebeck coefficient tensor, thermal conductivity tensor and electrical conductivity tensor, respectively	Element of Seebeck coefficient $S \propto T^m$ ( $m > 2$ ); carrier concentration $n \propto T^{3/2}$ ; $\kappa_L \propto T^3$ ; electrical power density $P_D = S^2 \Delta T^2 / (4R)$ ; topology-dependent $c_E$ , $R$ and $\eta$
Thermogalvanic <sup>b,c</sup>	Heat transfer, current and mass conservation equations alongside thermogalvanic and Soret effects <sup>23,140</sup> : $\frac{\partial T}{\partial t} + \rho C_p \nabla \cdot (\mathbf{u}T) + \nabla \cdot (-\kappa \nabla T) = Q,$ $(\mathbf{u} \cdot \nabla) \mathbf{u} = \nu \nabla^2 \mathbf{u} + \mathbf{g} \left(1 - \frac{\rho}{\rho_0}\right),$ $\nabla c = -c S_T \nabla T$	$\mathbf{u}$ is the bulk velocity vector, $\nu$ is viscosity, $\mathbf{g}$ is the gravity force, $c$ is the ion concentration and $S_T$ is the ion Seebeck coefficient; the slip condition at the wall is unconsidered; the electrolyte flow is laminar and incompressible, that is, $\nabla \cdot \mathbf{u} = 0$	$S(T)$ , $\mu(T)$ , $\eta(T)$ , $C_p(T)$ ; large $\Delta T$ , manipulative $\epsilon$ and $h_{\text{conv}}$ ; topology-dependent $c_E$ , $R$ , $P_D$ and $\eta$ ; $P_D = S^2 \Delta T^2 / (4R)$
Thermomagnetic <sup>b</sup>	Heat transfer and current conservation equation in conjunction with Faraday's law of electromagnetic induction <sup>25,141</sup> : $\rho C_p \frac{\partial T}{\partial t} + \rho C_p \mathbf{u} \cdot \nabla T + \nabla \cdot (-\kappa \nabla T) = Q,$ $\sigma \frac{\partial \mathbf{A}}{\partial t} + \nabla \times (\epsilon^{-1} \nabla \times \mathbf{A} - \mathbf{M})$ $-\sigma \mathbf{u} \times (\nabla \times \mathbf{A}) = \mathbf{J}_{\text{ex}}$ $\mathbf{n} \times \mathbf{H} = 0$	$\mathbf{A}$ is the magnetic vector potential, $\mathbf{M}$ is the magnetization vector, $\mathbf{J}_{\text{ex}}$ is the external current density, $\mathbf{n}$ is the normal vector, $\mathbf{H}$ is the magnetic field strength and $\epsilon$ is the permeability; the magnetic force in the non-conducting domain is modelled by integrating the Maxwell stress tensor variables	$\mathbf{M}(T)$ and $C_p(T)$ are temperature-dependent and topology-dependent variables; manipulative $\epsilon$ and $h_{\text{conv}}$ ; $V = N \cdot (\partial \Phi / \partial T) \cdot (\partial T / \partial t)$

<sup>a</sup>Solar-driven interfacial water evaporation with nonlinear heat distribution; <sup>b</sup>Transient heat harvesting triggered by temporal temperature changes ( $\partial T / \partial t$ ); <sup>c</sup>Steady-state heat harvesting driven by the spatial temperature gradient ( $\Delta T$ ).

systems, manipulating  $\omega$  and phonon–electron interactions across scales from nanoscale to macroscale could substantially modulate the thermodynamic properties and electric output potential.

## Atomic and nanoscale thermal nonlinearity

One common approach to understanding the structure–property correlation for the flexible manipulation of thermal and electrical transport in dielectrics is to introduce ultrafast control of structural dynamics in solid-state materials using light. In the ferroelectric community, one intriguing phenomenon lies in engineering the vibrational modes of lattice within bulk crystals using resonant mid-infrared light pulses<sup>58,59</sup> that beyond surface ferroelectricity<sup>60</sup>. Of particular interest is optically active phonon (incoming light-triggered high-frequency, strong modes) coupled with acoustic phonon (lattice vibrations at low-frequency, soft modes) influence the structural properties of ferroelectric materials. For instance, under ultrafast light pulse heating, by spatially separating the terahertz (THz) phonon creation region and lattice vibration region, the phonon dispersion is not confined to the hotspot near the sample surface but propagates with the travelling polariton throughout the entire bulk materials<sup>59</sup> (Fig. 3a). In

other words, the infrared heating is localized to a spot (near the sample surface), whereas phonon propagation in the ferroelectric is nonlocal. Moreover, incident high-frequency (THz) infrared irradiation induces a strong phonon mode within the hotspot, which couples with other phonons (soft modes at low frequencies) and drives the lattice vibration into the THz range. This coupling leads to nonlinear phononic manipulation of structural dynamics. Nonetheless, the current methodology primarily addresses nanoscopic and microscopic light-manipulated phonon propagation in the out-of-plane direction (that is, in the thickness direction), whereas the in-plane results are absent. Also, the exact influence of polaritons on induced polar charges in ferroelectric materials remains unclear. Additionally, to tune the structural dynamics of ferroelectrics using external light stimuli, other promising solutions for efficient heat harvesting are the flexible modulation of atomic resonance, lattice vibrations and strain propagation.

Aside from the external field modulation using light, high- $\kappa$  fillers (AlN, GaN nanoparticles) have been introduced into ferroelectric ceramics (lead zirconate titanate (PZT), bismuth sodium titanate) to boost  $\partial T / \partial t$  and  $p_{\text{pyro}}(T)$  (ref. 34). The introduction of GaN dopants promotes resonance vibration between Ga atoms and the ferroelectric

matrix, thereby facilitating the lattice vibration of  $\text{TiO}_6$  octahedra (Fig. 3b). This atomic lattice design not only increases  $\kappa_{\perp}$  but also boosts  $P_s$  (the element of spontaneous polarization), thus, leading to a high pyroelectric energy density of  $80 \mu\text{J cm}^{-3}$  at  $\Delta T = 2 \text{ }^\circ\text{C}$  with a matched load impedance. However, known ferroelectric materials are normally non-centrosymmetric, and the increased dopants of GaN nanoparticles may lead to inevitable current leakage owing to high  $\sigma$ . In this context, how the materials' anisotropy and dielectric loss of GaN-composited ferroelectric ceramics impact the  $P_s$  variation requires further examination.

Atomic staggered layer modulation in van der Waals single crystals via mechanical exfoliation (Fig. 3c) is another example that demonstrates the potential for harvesting environmental waste heat with high-performing thermoelectricity and flexibility<sup>52</sup>. Unlike thin films, inorganic bulk thermoelectrics suffer from stiffness and brittleness owing to ionic or covalent bond interactions, limiting their electrical and mechanical performance for adaptive heat harvesting at curved thermal sources. By contrast, the staggered layer formation via atom slips and exchanges (atomic structure rearrangement) around the van der Waals gap in single-crystalline (bismuth telluride) thin films has synergistic effects. First, the staggered layer is thought to be a donor impurity for tuning effective mass ( $m^*$ ) while minimally altering carrier transport ( $S \propto T^m$ ,  $S \propto m^*$  and  $n \propto T^{3/2}$ )<sup>61</sup>, bringing forth a high power factor. Second, atomic structure rearrangement is observed to redistribute nonlinear strain propagation across the van der Waals gap and lattice under external mechanical stimuli<sup>62</sup>, ensuring high bendability without compromising carrier mobility. Considering non-unity device topology alongside spectrum-selective solar heat absorption and regulation<sup>63,64</sup>, the  $\text{Bi}_2\text{Te}_3$  films achieve a high  $P_D$  of  $4.1 \text{ W m}^{-2}$  at

1 sun illumination. Although the developed staggered layer renders the typical brittle  $\text{Bi}_2\text{Te}_3$  crystalline flexible and shows general applicability in other layered compounds (such as tin selenide and bismuth selenide), further investigation is required to attain a high degree of control beyond atomic structure rearrangement<sup>65</sup> and in-depth phonon dispersion.

### Microscale thermal nonlinearity

Owing to the advanced manufacturing techniques in nanofabrication and microfabrication, nanoscale phenomena and effects can be effectively harnessed in dielectrics towards high-performing heat harvesting. One successful microfabrication demonstration involves engineering the dielectric surface with a non-flat texture (partially covered electrodes or nanoscale and microscale plasmonic metasurfaces) for solar heat absorption approaching the thermal limit. The partially covered electrode consists of multi-hole arrays on the polar dielectric, facilitating concurrent selective heat absorption and reflection and free charge collection during temporal temperature variations<sup>66,67</sup>. For instance, compared to a fully covered design, the micropatterned aluminium electrode (coverage area of 45%) on the poled polyvinylidene fluoride (PVDF) film boosts the open-circuit voltage by 380% owing to a delicate balance between enhanced thermal diffusion and electrostatic charge collection<sup>68</sup> (Fig. 3d). This strategy not only produces a high pyroelectric output but also reduces material usage with a lower electrode coverage area, thus, making heat harvesting highly cost-effective and sustainable.

In another approach, Au cubes with dimensions of hundreds of nanometres on top of an AlN film promote the pyroelectric photo-detection with a responsivity of  $0.18 \text{ V W}^{-1}$  and a rise time of 700 fs

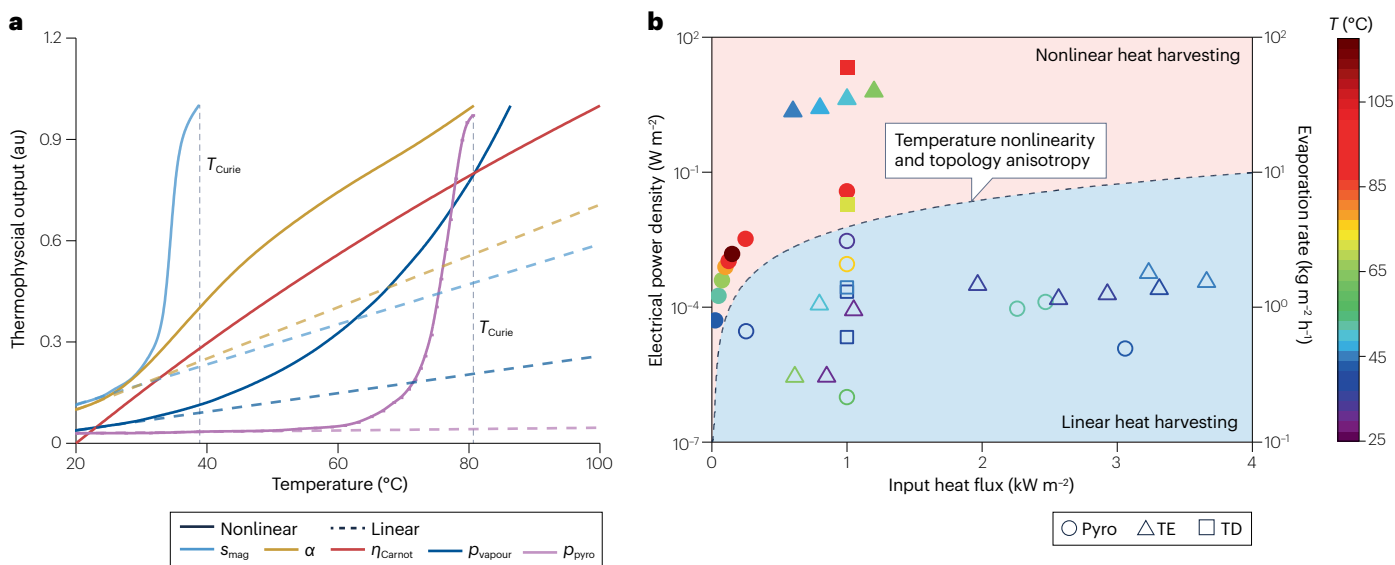


**Fig. 2 | Fundamentals and benchmarks of nonlinear heat harvesting.**

**a**, Temperature dependence of thermophysical output for different processes, with either linear or nonlinear dependence on temperature. Linear curves are set by the tangent of corresponding temperature-dependent figures of merit at  $20 \text{ }^\circ\text{C}$  and represent the limitation of thermophysical output under a linear process or low temperature (for example, bulk solar vapourization near the room temperature). **b**, Benchmarks of electrical power density (left axis) and evaporation rate (right axis) at various input heat fluxes. The outputs of nonlinear heat harvesters (solid symbols) are much higher than those of linear harvesters

(open symbols). Circles (pyroelectric heat harvesters, 'pyro')<sup>16,40–46</sup>, triangles (thermoelectric heat harvesters, 'TE')<sup>47–52</sup> and squares (thermal desalination, 'TD')<sup>15,53–55</sup> are coloured with respect to experimental temperatures (indicated by the colour bar) of measured electrical power density and evaporation rates. The dashed line indicates how to transform heat harvesting from linear to nonlinear processes via temperature nonlinearity and topology anisotropy.  $\alpha(T)$ , absorbance<sup>36</sup>;  $\eta_{\text{Carnot}}(T)$ , Carnot efficiency, calculated using the formula of  $\Delta T/T_{\text{H}}$  in the unit of Kelvin;  $p_{\text{vapour}}(T)$ , vapour saturation pressure<sup>15</sup>;  $p_{\text{pyro}}(T)$ , pyroelectric coefficient<sup>85</sup>;  $S_{\text{mag}}(T)$ , magnetic entropy change<sup>25</sup>.

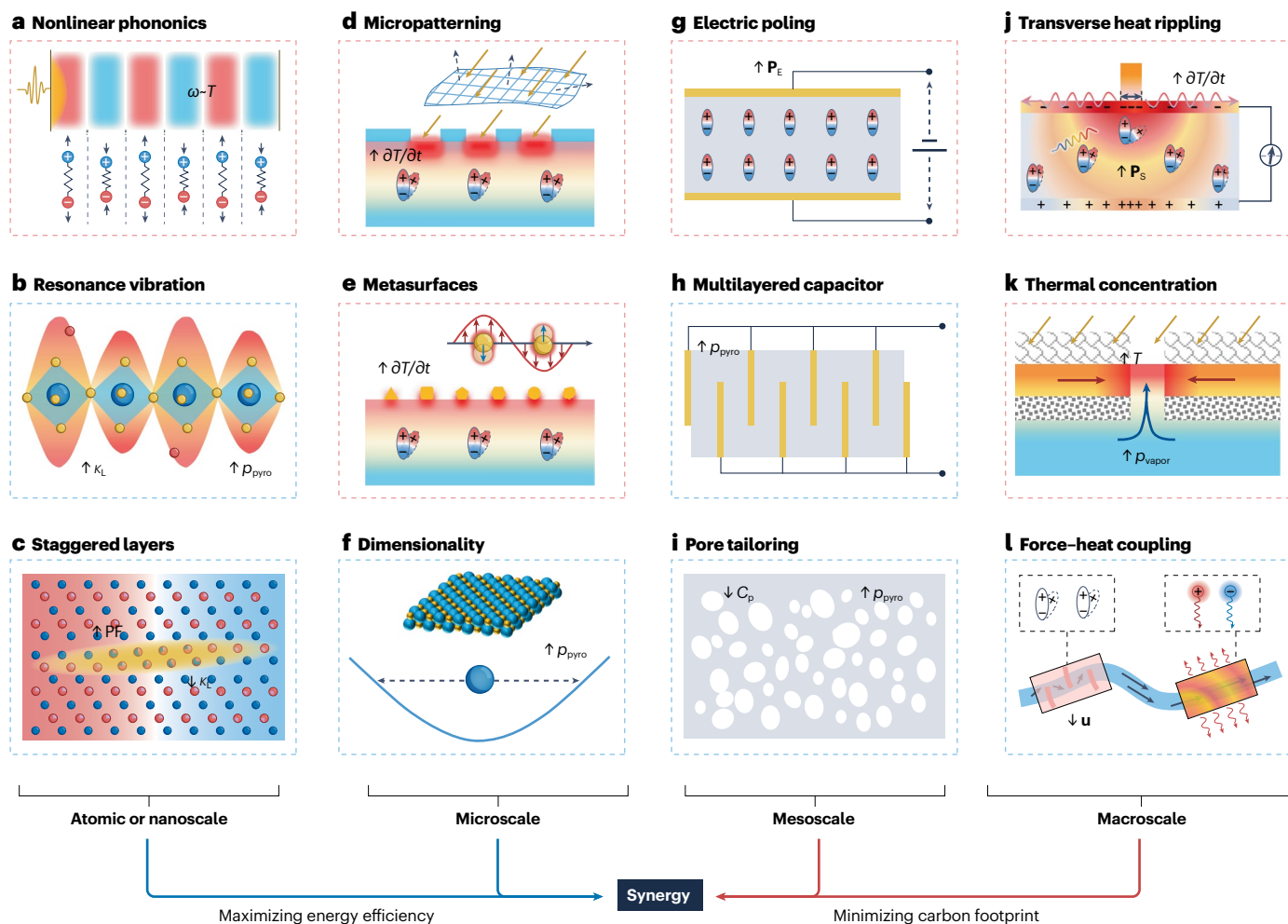


**Fig. 3 | Multiscale structure topology and mechanisms for nonlinear heat harvesting.** **a–c**, Atomic or nanoscale heat manipulation: ultrafast mid-infrared light pulses trigger nonlinear phonics with high-frequency ( $\omega$ ) mode in ferroelectricity<sup>59</sup> (panel **a**); resonance vibration between high thermal conductivity ( $\kappa_L$ ) filters and ferroelectric matrix for increased pyroelectricity ( $p_{\text{pyro}}$ )<sup>34</sup> (panel **b**); and boosted thermoelectric power factor (PF) and decreased thermal conductivity ( $\kappa_L$ ) with staggered layers<sup>52</sup> (panel **c**). **d–f**, Microscale heat modulation: partially covered electrodes with micropatterning for increased temporal temperature change ( $\partial T/\partial t$ ) and pyroelectricity<sup>68</sup> (panel **d**); localized surface plasmon resonance and metasurface-boosted temporal temperature change ( $\partial T/\partial t$ ) for improved pyroelectricity<sup>69</sup> (panel **e**); giant pyroelectricity ( $p_{\text{pyro}}$ ) tuned by 3D-to-2D dimensionality<sup>73</sup> (panel **f**). **g–i**, Mesoscale heat regulation: electric field-driven polarization ( $P_E$ ) with aligned dipoles in pyroelectric thin films<sup>17</sup> (panel **g**); multilayered capacitor-boosted pyroelectricity ( $p_{\text{pyro}}$ )<sup>75</sup> (panel **h**); micropore tailoring for decreased specific

heat capacity ( $C_p$ ) and increased pyroelectricity ( $p_{\text{pyro}}$ )<sup>79</sup> (panel **i**). The mesoscale specifies the dimension or field modulation at the mesoscopic device level. **j–l**, Macroscale thermal engineering: transverse pyroelectricity with large spontaneous polarization ( $P_S$ ) and temporal temperature change ( $\partial T/\partial t$ ) gained from spatial heat decoupling<sup>80</sup> (panel **j**); nonlinear thermal desalination with a high temperature ( $T$ ) and vapour saturation pressure ( $p_{\text{vapour}}$ ) through thermal concentration<sup>88</sup> (panel **k**); thermo-fluid energy harvesting with the introduction of piezoelectric harvesters (for slowing down the velocity ( $u$ ) of moveable fluids) and thermoelectric generators<sup>91</sup> (panel **l**). Dashed light red blocks, nonlinear heat harvesting at applied electric, optical and/or thermal field modulations. Dashed light blue blocks, structure topology modulation of materials, devices or systems.  $\omega$ , phonon frequency;  $\kappa_L$ , lattice thermal conductivity;  $p_{\text{pyro}}$ , pyroelectric coefficient;  $P_E$ , vector of electric field-driven polarization;  $P_S$ , vector of spontaneous polarization;  $u$ , vector of velocity of movable fluids.

(refs. 69–71), by means of localized surface plasmons which decay at femtosecond timescales and nonlinear heat generation through electron–phonon scattering (Fig. 3e). Noticeably, these designs are implemented at room temperature in the absence of denoising and cryogenic calibration, offering modularity and scalability for practical applications.

In addition, the dimensionality effect of pyroelectric nanowires and nanomembranes has a critical role in manipulating heat transport and thermal energy harvesting performance<sup>72–74</sup>. For example, when polar materials approach the 2D crystalline limit, the dimensionality effect substantially alters phonon dynamics, leading to improved pyroelectricity (Fig. 3f). Specifically, the reduced limitation of atomic

displacement along the thickness direction in a 2D system has experimentally demonstrated an augmented  $p_{\text{pyro}}(T)$  (ref. 73). Interestingly, this phenomenon is also observed in van der Waals layered  $\text{In}_2\text{Se}_3$ , quasi-van der Waals  $\text{CsBiNb}_2\text{O}_7$  and ionic  $\text{ZnO}$  crystals. In theory, the achieved giant  $p_{\text{pyro}}(T)$  via dimensionality effects in nanomembranes is attributed to electron–phonon renormalization owing to thickness-dependent mean square displacement<sup>74</sup>. However, it is not yet fully clear how  $a$  and  $P_s$  anisotropy change with thickness variation. Meanwhile, the competitive mechanism between the varied thickness and thermal penetration depth under laser heating is unexplored. In-depth examinations could ensure a precise measurement of  $p_{\text{pyro}}(T)$  and deepen the understanding of polarization evolution.

## Mesoscale thermal nonlinearity

Aside from tailoring the material properties at atomic, nanoscale and microscale; at the mesoscopic level, the thermophysical output of pyroelectrics can be manipulated nonlinearly from the viewpoint of material porosity and device topology. Normally, the electrical and thermal transport behaviours of polar materials are related to the electric field vector  $\mathbf{E}$  and topology at a given temperature. Explicitly, according to the pyroelectric fundamentals (Table 1), a large electric polarization change (or  $p_{\text{pyro}}$ ) can be achieved through thermodynamic cycles performed in the temperature–entropy ( $T$ – $s$ ) plane associated with the polarization–electric field ( $P$ – $E$ ) plane, which is also known as nonlinear pyroelectrics (the element of electric field-driven polarization  $P_E \neq 0$ )<sup>75</sup>. In other words, the harvested energy density (that is, the integral of electric polarization or dielectric displacement versus the electric field) of a pyroelectric device can be boosted by adopting a thermodynamic cycle (for example, Ericsson cycle or Olsen cycle) involving two isothermal and two isoelectric processes<sup>47,75,76</sup>. For instance, the introduction of an external  $\mathbf{E}$  not only facilitates electric dipole moment (ferroelectric domain wall) alignment but also suppresses the dielectric response towards a large pyroelectric energy density<sup>77,78</sup> (Fig. 3g). Moreover, electric field-driven dipole moment changes, together with multilayered capacitors (Fig. 3h), have been used in pyroelectric heat harvesting, engendering a joule-level energy output<sup>47,75</sup>. The reduction of dielectric thickness in multilayered capacitors not only increases capacitance and  $\mathbf{E}$  across a thin layer of active materials between two electrodes but also increases device density and packaging compatible with emerging electronics. Additionally, porosity tailoring at the mesoscale offers a viable solution to tune  $\kappa_t$  (or  $C_p$ ) and  $\mathbf{E}$ , especially for poled PVDF polymers. For example, compared to commercial dense films, porous PVDF films exhibit a lower  $C_p$ , resistivity and a higher  $P_s$  (Fig. 3i), which is beneficial for nonlinear thermal response towards specific applications<sup>79</sup>. These materials, referred to as porous-architected materials in ferroelectrics<sup>80,81</sup> and thermoelectrics<sup>82</sup>, are burgeoning research topics that synergistically integrate mechanical and thermal nonlinearity with cost-effectiveness for sustainable energy harvesting. Nonetheless, maintaining an ultrahigh  $\mathbf{E}$  across ultrathin films may result in ferroelectric fatigue owing to charge injection, dielectric breakdown and current leakage<sup>83</sup>. Addressing the sustainability of electric field-driven polarization and minimizing current leakage after numerous thermal cycles remains challenging.

## Macroscale thermal nonlinearity

In prototype-scale or system-level heat harvesting, thermal nonlinearity is also crucial for manipulating heat and mass transport towards matchable energy flow between the thermal sources (which may be non-flat or

curved, vibrational or quasi-static) and energy harvesters. Non-static waste heat can be efficiently converted into electricity using transverse pyroelectricity of polar materials (Fig. 3j). For example, incoming solar heat is confined at a hotspot to trigger thermal rippling from the irradiated area to the circumjacent regions across the in-plane direction, leading to giant polarization ripples and pyroelectric dipole moment changes<sup>16,84</sup>. In other words, the spatial decoupling of heat generation from its transverse propagation offers a synergistic increase in  $\partial T/\partial t$  and  $p_{\text{pyro}}(T)$  around the  $T_{\text{Curie}}$ , leading to a fivefold increase in  $\eta$  compared to conventional designs<sup>16,84,85</sup>. Owing to the spatiotemporal tuneability of  $T(x,y,z,t)$  through the deployment of asymmetrical configurations with inhomogeneous  $\kappa$ , the large  $\partial T(x,y,z,t)/\partial t$  makes it possible to increase  $P_s$  by approximately 900% compared to conventional designs. These optically and thermally configured heat harvesting devices also offer feasibility for modular and prototype integration towards a high  $P_D$  of 38 mW m<sup>-2</sup> at 1 sun illumination, comparable to solar organic thermoelectrics<sup>47,49</sup> and ferro-photovoltaics<sup>86,87</sup>.

In addition, thermal nonlinearity has been adapted in environmental waste heat recovery owing to the nonlinear FOMs of heat harvesting materials (Fig. 2a). For instance, a layered solar absorber-regulator with a distributed hole layout is capable of thermally concentrating heat flow for localized water boiling (100 °C) and steam generation with a peak efficiency of 73% (ref. 88) (Fig. 3k). These results are mainly ascribed to the thermal design at the water–air interface that not only maximizes the volume of air for vapour diffusion per distributed circular slot but also contributes to thermal concentration and localization alongside the exponential  $p_{\text{vapour}}(T)$  (refs. 15,89,90) (Fig. 2a). As a result, the overall  $m_{\text{evp}}$  during the nonlinear process is far beyond that of the conventional bulk solar vapourization (Fig. 2b).

In another approach, owing to the thermal nonlinearity observed in the thermodynamic cycles of a thermo-fluid system (Fig. 3l), segmented mechanical and thermal energy harvesters can modulate the thermophysical properties ( $T(x,y,z,t)$ ) and velocity vector of movable fluid ( $\mathbf{u}$ ) of waste thermo-fluid via radial piezoelectric devices. This modulation facilitates heat conduction to annular thermoelectric generators, resulting in an increased  $P_D$  of 158% (ref. 91). Nevertheless, the macroscopic thermal stability, durability, strain distribution and techno-economics of prototype-scale heat harvesting systems under nonlinear processes need further study.

## Synergy of scale-to-scale thermal nonlinearity

Compared to heat harvesting strategies through thermal manipulation on a single scale, the synergy of scale-to-scale thermal nonlinearity in conjunction with applied multiphysical fields at a steady or transient state could be more effective in maximizing energy efficiency and minimizing carbon footprint. However, the low transferability and scalability of exceptional FOMs gained at the nanoscale make device implementations with macroscale temperature nonlinearity challenging both in spatial and temporal domains. Fortunately, using dual (or multiple) thermal nonlinearities – such as micro or nanofabrication combined with macroscale device topology<sup>52,92</sup> (Fig. 3c,k), mesoscale thinning alongside electric poling<sup>8,75</sup> (Fig. 3g,h) and microscale dipole moment shifts coupled with macroscale thermal decoupling<sup>73</sup> (Fig. 3f,j) – has been demonstrated to boost thermoelectric and pyroelectric  $P_D$  by one to two orders of magnitude. These strategies outperform approaches that solely rely on nanoengineered materials or micropatterned electrode configurations. These advances are mainly attributed to the synergistic increase of  $T$ -dependent FOMs alongside  $\partial T/\partial x$  or  $\partial T/\partial t$  that differ from the sum of benefits from each nonlinearity individually.

To quantify how specific nonlinearities and scale manipulations advance the potential improvements and implications of heat harvesting technologies, detailed output increments alongside the technology readiness level (TRL) are tabulated in Table 2. TRL is a measurement of the maturity of a particular technology ranging from level 1 (basic principles observed) to level 9 (actual system proven through successful operations). Notably, a substantial output enhancement of up to one to two orders of magnitude (consistent with Fig. 2b) can be achieved at the prototype level with technological feasibility (TRL  $\geq 5$ ) through the implementation of micro-to-macroscale and scale-to-scale thermal nonlinearities. More importantly, in view of techno-economics and sustainability (Table 3), increasing  $P_D$  via rational thermal design in heat harvesting materials and devices leads to a reduction of raw material usage, electricity consumption and carbon emission during manufacturing of materials or device. This approach provides an unexpected but feasible solution to align synthesis of materials, device co-design, and system integration across multiscale thermal nonlinearities, thus, promoting sustainable and affordable heat harvesting that goes beyond nonlinear systems.

## Outlook

To advance the future of nonlinear heat harvesting, it is essential to address the following key challenges.

### The correlation between structure topology and physical transport

The giant changes in thermophysical properties of heat harvesting materials typically occur around  $T_{\text{Curie}}$  owing to temperature-driven phase transitions. Examples include the sharp increase in  $p_{\text{pyro}}$  resulting

from the FE–PE phase transition, the variation in magnetic entropy around  $T_{\text{Curie}}$  during the FM–PM phase transition, and the unusual change of  $S(T)$  and  $C_p(T)$  owing to low-to-high- $T$  structural phase transition. Therefore, to improve heat harvesting performance, it is recommended to capture waste heat around  $T_{\text{Curie}}$  and exploit phase transitions<sup>8,75</sup>.

Unfortunately, striking a delicate balance between material candidates and complementary thermal sources is challenging. First, the thermal and electrical transport properties of materials are  $T$ -dependent and correlated with crystal structures<sup>93–96</sup>. As such, improving  $\eta$  necessitates exploring phase transition theories to decrease the  $T_{\text{Curie}}$  to near room temperature<sup>75</sup>, sustain the built-in electric field across Schottky interfaces around  $T_{\text{Curie}}$  (ref. 95), or develop multiple phase transitions (or  $T_{\text{Curie}}$ ) over a wide temperature range<sup>17</sup>, especially for temporal or non-static heat harvesting (for example, in pyroelectrics or thermomagnetics)<sup>97</sup>. For spatial or thermoelectric heat harvesting, the charge current is generated in the direction of  $\Delta T$  (the longitudinal Seebeck effect), wherein the inevitable thermal and electrical contact at the hot side results in low  $\eta$  and stability. Some key challenges include but are not limited to pushing the  $S(T)$  beyond the theoretical limit predicted by the Goldsmid–Sharp equation (that is,  $S(T)_{\text{max}} \approx \frac{E_g}{2eT_{\text{max}}}$ ) (ref. 98); maintaining a high average power factor or ZT over a wide temperature range (at a given  $\Delta T$ ) with appropriate carrier concentration<sup>99,100</sup>; and transitioning thermoelectric heat harvesting in the absence of hot-side contact technology (or junctionless topology), for example, by generating the charge current in the perpendicular direction of  $\Delta T$  alongside an applied magnetic field (known as transverse thermoelectricity)<sup>101,102</sup>. In addition, the electrothermal

**Table 2 | State-of-the-art nonlinear heat harvesting technologies with quantitative output increments**

Thermal nonlinearities	Technologies	Thermal field	Method or mechanism	Nonlinear FOM	Output increment	TRL <sup>a</sup> (1–9)
Atomic and nanoscale	Pyroelectric	Temporal	Nonlinear phononics <sup>59</sup>	$\omega \sim T$	Unknown	1
			Resonance vibration <sup>34</sup>	$p_{\text{pyro}}, K$	2.8 ( $p_{\text{pyro}}$ )	3
	Thermoelectric	Spatial	Staggered layers <sup>52</sup>	$S, \sigma, \kappa$	0.8 (ZT)	5
Microscale	Pyroelectric	Temporal	Micropatterning <sup>68</sup>	$\partial T / \partial t$	10.8 ( $P_D$ )	4
			Metasurfaces <sup>69</sup>	$\partial T / \partial t, p_{\text{pyro}}$	Unknown	4
			Dimensionality <sup>73</sup>	$p_{\text{pyro}}, K$	105.7 (FOM)	2
Mesoscale	Pyroelectric	Temporal	Electric poling <sup>17,75</sup>	$\mathbf{P}_E$	4.5 ( $p_{\text{pyro}}$ )	8
			Multilayered capacitors <sup>75</sup>	$p_{\text{pyro}}, K$	13.0 ( $P_D$ )	7
			Pore tailoring <sup>79</sup>	$p_{\text{pyro}}, K$	0.7 (FOM)	4
	Thermoelectric	Spatial	Geometric printing <sup>92,142,143</sup>	$n, \kappa, \Delta T$	1.3 ( $P_D$ )	5
Macroscale	Pyroelectric	Temporal	Transverse heat rippling <sup>16</sup>	$\partial T / \partial t, \mathbf{P}_S$	5.4 ( $P_D$ )	6
	Thermal desalination	Spatial	Thermal regulation <sup>15,88</sup>	$T, p_{\text{vapour}}$	>0.5 ( $\eta$ )	7
	Thermoelectric	Spatial, temporal	Force–heat coupling <sup>91</sup>	$\mathbf{u}$	1.6 ( $P_D$ )	6
Scale-to-scale	Pyroelectric	Temporal	Electric poling and multilayered capacitors <sup>75</sup>	$\mathbf{P}_E, p_{\text{pyro}}, K$	>30 ( $P_D$ )	6
	Thermoelectric	Spatial	Nanoscale and macroscopic thermal designs <sup>52</sup>	$\kappa, \Delta T$	3.2 ( $P_D$ )	5

$\kappa$ , thermal conductivity;  $n$ , carrier concentration;  $\eta$ , energy efficiency;  $\sigma$ , electrical conductivity;  $\omega$ , phonon frequency; FOM, figure of merit;  $P_D$ , power density;  $\mathbf{P}_E$ , vector of electric field-driven polarization;  $p_{\text{pyro}}$ , pyroelectric coefficient;  $p_{\text{vapour}}$ , vapour saturation pressure;  $S$ , Seebeck coefficient; TRL, technology readiness level;  $\mathbf{u}$ , velocity vector of movable fluids; ZT, thermoelectric figure of merit. <sup>a</sup>The TRL of heat harvesting technologies is quantified in the consideration of technology, product development, product definition or design, competitive landscape, team, go-to-market, and manufacturing or supply chain, according to TRL calculators and self-assessment tools<sup>19,144</sup>.

**Table 3 | Contribution of nonlinear heat harvesting towards the UN SDGs**

UN SDGs	Relevant targets <sup>145</sup>	Technology-led innovations	Solutions
 6 CLEAN WATER AND SANITATION	6.1: Safe and affordable drinking water, 6.3: Improve water quality, wastewater treatment and safe reuse, 6.4: Increase water-use efficiency and ensure freshwater supplies, 6.7: Expand water and sanitation support to developing countries	Thermal desalination for affordable drinking water supplies <sup>14,64</sup> ; solar steam generation for high-temperature and high-pressure sanitation <sup>146</sup>	Thermal-driven water-energy harvester <sup>64</sup> ; high-temperature, high-pressure solar steam generator <sup>146</sup>
 7 AFFORDABLE AND CLEAN ENERGY	7.2: Increase global percentage of renewable energy, 7.3: Double the improvement in energy efficiency, 7.4: Promote access to research, technology and investments in clean energy	Nonlinear pyroelectrics for temporal waste heat harvesting <sup>16,75</sup> ; non-unity thermoelectrics for spatial waste heat recovery <sup>63</sup>	Transverse pyroelectric generation system <sup>16</sup> ; temperature-adaptive radiative coating <sup>26</sup> ; modular and flexible thermoelectric device <sup>63</sup> ; climate-resilient non-planar energy harvester <sup>84</sup>
 9 INDUSTRY, INNOVATION AND INFRASTRUCTURE	9.1: Develop sustainable, resilient and inclusive infrastructures, 9.2: Promote inclusive and sustainable industrialization, 9.4: Upgrade all industries and infrastructures for sustainability, 9.5: Enhance research and upgrade industrial technologies	Waste energy harvesting for buildings using pyroelectrics, thermoelectrics and triboelectrics <sup>64</sup> ; zero-carbon or zero-energy buildings with the use of climate-resilient water and energy harvesting technologies <sup>26,147</sup> ; spatially spectrum-selective solar absorption and reflection for thermoelectric heat harvesting <sup>52</sup> ; geometric heat transfer with reduced material usage and electricity consumption towards lab-to-industry sustainable manufacturing, decarbonization, and environmental, social and governance (ESG) response <sup>53</sup> ; scalable, low-cost, eco-friendly polar materials for transverse pyroelectric heat harvesting <sup>84</sup>	
 11 SUSTAINABLE CITIES AND COMMUNITIES	11.3: Inclusive and sustainable urbanization, 11.6: Reduce the environmental impact of cities, 11.a: Support least developed countries in sustainable and resilient building		
 12 RESPONSIBLE CONSUMPTION AND PRODUCTION	12.2: Sustainable management and use of natural resources, 12.5: Substantially reduce waste generation, 12.6: Encourage companies to adopt sustainable practices and sustainability reporting		
 13 CLIMATE ACTION	13.1: Strengthen resilience and adaptive capacity to climate-related disasters, 13.2: Integrate climate change measures into policy and planning		

Icons reproduced from United Nations Sustainable Development Goals (UN SDGs): <https://www.un.org/sustainabledevelopment/>. The content of this publication has not been approved by the United Nations and does not reflect the views of the United Nations or its officials or Member States.

response and evolution of heat harvesting materials at multiple scales under phase transitions need to be examined.

### Dominant factor in enhanced nonlinear heat harvesting

From the perspective of thermodynamic energy conversion, the  $\eta$  of a heat engine consists of two components, that is,  $\eta = \eta_{\text{Carnot}}\eta_r$ . The former is determined by the initial and boundary conditions, whereas the latter is known as the irreversibility of heat engines (relative Carnot efficiency or reduced efficiency) and is governed by the thermophysical metrics or FOMs of materials and device architectures. Because most heat harvesting materials have a non-centrosymmetric structure, the performance metric is asymmetric and varies substantially in the structure orientations and in-plane or out-of-plane directions<sup>103,104</sup>. Therefore, especially for nonlinear processes, it is necessary to quantify the different contributions to the net  $\eta$  (such as FOMs, the intensity of  $\partial T/\partial x$  or  $\partial T/\partial t$ , and anisotropy) to identify the dominant factors for flexibly and sustainably manipulating the transport properties of the working media in a heat harvesting system. This quantification can be achieved through various means, including performing multiscale modelling and computation to understand the transport kinetics of energy carriers (such as phonons, electrons and ions), probing ultrafast interaction phenomena between electrons and phonons with multidimensional (four-dimensional) high-resolution microscopy, conducting multiphysical measurements in different orientations or directions, monitoring  $T(x,y,z,t)$  evolution in both spatial and temporal domains, and excluding non-primary or secondary effects. These clarifications could bridge the physical understanding between transport fundamentals and experimental implementations of heat harvesting materials for boosted thermophysical output and on-demand applications.

### Physics-guided machine learning for advanced synthesis of materials and device co-design

Traditionally, synthesis of materials and device co-design are trial-and-error and focused on empiricism. This approach restrains the discovery of new materials and makes device fabrication time consuming, cost-ineffective and unsustainable. Fortunately, prediction and synthesis of materials may be reshaped by the use of quantum theory, geometric theory, cross-scale computing, multiphysical field modelling, machine learning, and databases of materials from the literature. These approaches open new doors for the design of artificial materials with extreme properties beyond those of natural materials<sup>105,106</sup>, the optimization of material synthesis processes with cost-effectiveness and scalability in mind<sup>107</sup>, and the development of device performance with adaptiveness and diversification<sup>63</sup>. On one hand, physics-assisted modelling with multiphysical field decoupling at multiple scales provides valuable guidelines for device co-design. For example, all-scale hierarchical architectures or high-entropy engineering for full-spectrum phonon scattering<sup>108,109</sup>, non-unity and/or non-cuboid topology design for decoupled macroscopic thermal and electrical transport<sup>63,92</sup>, interface engineering for thermal and strain fatigue resilience<sup>110,111</sup>. On the other hand, machine learning, phase diagram calculation and high-throughput computation offer an in-depth understanding of structure–property correlations, unlocking new possibilities beyond classical mechanics and conventional empirical-centralized or semi-empirical approaches. Examples include data-driven prediction of new thermoelectric materials<sup>112–115</sup>, screening search for thermal interface materials<sup>111,116</sup>, and inverse design of multiphysical metamaterials and devices<sup>105,117,118</sup>. The synergy between physics-guided modelling and machine learning presents a positive feedback loop, accelerating the manufacturing

of materials and devices towards the development phase of emerging heat harvesting technologies from a scientific or technological point of view<sup>119</sup>.

## Large-scale device fabrication and integration

To sustain milliwatt-level consumer electronics or kilowatt-scale daily power supply through waste heat harvesting, advanced device fabrication with integrated mature technologies (TRL  $\geq 6$ ) is essential<sup>120,121</sup>. Recent advances in additive manufacturing have made it possible to fabricate architected materials and structures (such as metamaterials and metastructures) with  $\kappa$  beyond that of natural materials (23 mW m<sup>-1</sup> K<sup>-1</sup> (air) to 429 W m<sup>-1</sup> K<sup>-1</sup> (silver)). According to the macroscopic heat transfer equation,  $T(x,y,z,t)$  can be manipulated via active thermal convection (movable fluids) or passive thermal resistance (variable heat transport area). These artificial thermal conduction phenomena with an effective  $\kappa$  of up to 1915 W m<sup>-1</sup> K<sup>-1</sup> have been experimentally demonstrated through the deployment of thermal metamaterials<sup>122–124</sup>. Moreover, guided by the effective medium theory, ultralow  $\kappa$  close to the air has been achieved in architected or porous air-filled materials, owing to the lattice architecture design and additive manufacturing. The ultrahigh or ultralow  $\kappa$  achieved in thermal metamaterials and metastructures offers a new avenue not only for manipulating the transport kinetics of working media (such as electrons, phonons and so on) in thermodynamic heat engines but also for modulating the intensity of  $\partial T/\partial t$  and  $\partial T/\partial x$ . For instance, architected thermoelectric legs with macroscopic thermal designs increase thermal resistance while lowering electrical resistance, thus, substantially boosting  $P_D$  at a consistent thermal input<sup>92,125</sup>.

However, the challenge lies in transitioning these proof-of-concept technologies (TRL  $\leq 3$ ) from the laboratory into industrial production (TRL  $\geq 7$ ), necessitating physical modelling and techno-economic analysis. For example, segmented and architected thermoelectrics have demonstrated high  $\eta$ , but the path to mass production (for instance, via current Bi<sub>2</sub>Te<sub>3</sub> manufacturing technologies) needs further exploration, such as validation of manufacturing compatibility and adaptiveness for on-demand physical layouts, mathematical formulation of fatigue analysis and service lifetime prediction. In addition, thermal and/or optical concentration introduces intricacy and instability into solar heat harvesting systems, and there is a need to investigate how to upgrade the heat quality via concentration-free designs (such as optical or thermal metasurfaces<sup>123,126</sup>, or mechanical metamaterials<sup>125,127,128</sup>) both in fundamentals and experiments. Meanwhile, integrating heat harvesting technologies in tandem with other energy storage systems and circuit interfaces (synergy and complementarity across multiple energy resources) could stabilize electrical output and overcome the intermittency and variability of environmental waste thermal sources.

## Techno-socioeconomic sustainability of nonlinear heat harvesting

The ultimate goal of nonlinear heat harvesting is to fundamentally and techno-economically advance the energy transition from fossil fuels to renewable and sustainable energy sources at an industrial scale by using clean energy technologies. To date, thermoelectric devices with Bi<sub>2</sub>Te<sub>3</sub> materials have been commercialized and found practical implications in environmental waste heat recovery, in the form of body heat<sup>129–131</sup>, automotive exhaust waste heat<sup>132,133</sup> and waste thermo-fluids of industrial factories<sup>91</sup>. Unfortunately, the cost-effectiveness of thermoelectric devices is still limited by raw materials that are expensive (approximately US\$110 kg<sup>-1</sup> for bismuth telluride) and of low abundance

(0.2 ppm in bismuth, 0.001 ppm in telluride and 0.2 ppm in antimony, by weight)<sup>134,135</sup>, by low-efficient device configurations<sup>63</sup> and by inadaptable heat exchangers<sup>136</sup>.

For pyroelectric heat harvesting, the cost of raw materials, the attainability of thermal cycling, and the adaptability of  $T_{Curie}$  versus the temporal thermal source are crucial for maximizing cost-effectiveness. Currently, pyroelectrics materials are primarily limited to ceramic oxides (such as PZT and lead magnesium niobate–lead titanate) and polymers (such as PVDF-based fluoropolymers, copolymers and terpolymers)<sup>7,85</sup>. Among them,  $\beta$ -PVDF, which is synthesized via commercial technologies (such as sol-gel and spin-coating methods) with tailorable ferroelectricity and compliance with restriction of hazardous substance or lead-free regulations, offers potential scalability and sustainability for low-grade waste heat harvesting.

For passive thermal cycling, solar-heat manipulators (such as planar thermal or optical lens)<sup>16</sup>, thermal metasurfaces (micro-structured selective light absorbance or emittance)<sup>69</sup> and phase-change metamaterials with  $T$ -dependent absorbance (such as vanadium dioxide)<sup>26</sup> are promising ways to maximize the intensity of  $\partial T/\partial t$ .

Transforming clean energy technologies from laboratory to industry and meeting the UN SDGs demands a collaborative and collective effort involving academia, industry and policymakers (environmental, social and governance (ESG)). Aligning technology priorities with ESG investing, energy policy and local climate targets, especially in developing countries and remote regions, is crucial. For instance, achieving a comprehensive physical estimation of the techno-socioeconomic aspects, carbon footprint and energy savings associated with the deployment of non-unity topologies in the thermoelectric industry is essential.

Published online: 21 October 2024

## References

1. Johnson, I., Choate, W. T. & Davidson, A. *Waste Heat Recovery, Technology and Opportunities in U.S. Industry*. OSTI ID 1218716 (BCS, Inc., 2008).
  2. International Energy Agency. *Energy Efficiency 2022* (IEA, 2022).
  3. International Energy Agency. *Key World Energy Statistics 2021* (IEA, 2021).
  4. Zhou, C. et al. Polycrystalline SnSe with a thermoelectric figure of merit greater than the single crystal. *Nat. Mater.* **20**, 1378–1384 (2021).
  5. Yan, Q. & Kanatzidis, M. G. High-performance thermoelectrics and challenges for practical devices. *Nat. Mater.* **21**, 503–513 (2022).
  6. He, J. & Tritt, T. M. Advances in thermoelectric materials research: looking back and moving forward. *Science* **357**, 1369 (2017).
  7. Bowen, C. R. et al. Pyroelectric materials and devices for energy harvesting applications. *Energy Environ. Sci.* **7**, 3836–3856 (2014).
  8. Yang, Y. Pyroelectricity gain in multilayers. *Nat. Energy* **7**, 1007–1008 (2022).
  9. Li, W. et al. Improper molecular ferroelectrics with simultaneous ultrahigh pyroelectricity and figures of merit. *Sci. Adv.* **7**, eabe3068 (2021).
  10. Zhao, F. et al. Highly efficient solar vapour generation via hierarchically nanostructured gels. *Nat. Nanotechnol.* **13**, 489–495 (2018).
  11. Tu, Y. et al. Plausible photomolecular effect leading to water evaporation exceeding the thermal limit. *Proc. Natl Acad. Sci. USA* **120**, e2312751120 (2023).
  12. Peng, J. et al. New cambered-surface based drip generator: a drop of water generates 50  $\mu$ A current without pre-charging. *Nano Energy* **102**, 107694 (2022).
  13. Maharjan, P. et al. Brachistochrone bowl-inspired hybrid nanogenerator integrated with physio-electrochemical multisensors for self-sustainable smart pool monitoring systems. *Adv. Energy Mater.* **13**, 2203849 (2023).
  14. Ding, T., Zhou, Y., Ong, W. L. & Ho, G. W. Hybrid solar-driven interfacial evaporation systems: beyond water production towards high solar energy utilization. *Mater. Today* **42**, 178–191 (2021).
  15. Dongare, P. D., Alabastri, A., Neumann, O., Nordlander, P. & Halas, N. J. Solar thermal desalination as a nonlinear optical process. *Proc. Natl Acad. Sci. USA* **116**, 13182–13187 (2019).
- This work utilizes the exponential temperature dependence of water vapour saturation pressure under nonlinear heating to achieve a high solar-driven interfacial water evaporation rate.**
16. Zhou, Y. et al. Giant polarization ripple in transverse pyroelectricity. *Nat. Commun.* **14**, 426 (2023).
- This work reveals the thermal nonlinearity of spontaneous polarization changes in general pyroelectrics via transverse heat generation and propagation decoupling.**

17. Pandya, S. et al. Pyroelectric energy conversion with large energy and power density in relaxor ferroelectric thin films. *Nat. Mater.* **17**, 432–438 (2018).
18. Zhang, Y. et al. Thermal energy harvesting using pyroelectric-electrochemical coupling in ferroelectric materials. *Joule* **4**, 301–309 (2020).
19. Szigeti, B. Temperature dependence of pyroelectricity. *Phys. Rev. Lett.* **35**, 1532–1534 (1975). **This work reveals the cubic temperature dependence of primary and secondary pyroelectricity owing to the anharmonic potential.**
20. Chang, C. et al. 3D charge and 2D phonon transports leading to high out-of-plane ZT in n-type SnSe crystals. *Science* **360**, 778 (2018).
21. Lee, S. et al. Anomalously low electronic thermal conductivity in metallic vanadium dioxide. *Science* **355**, 371–374 (2017).
22. Yu, B. et al. Thermosensitive crystallization-boosted liquid thermocells for low-grade heat harvesting. *Science* **370**, 342–346 (2020).
23. Han, C. G. et al. Giant thermopower of ionic gelatin near room temperature. *Science* **368**, 1091–1098 (2020). **This work investigates the synergy of thermogalvanic and thermodiffusion effects in improving ionic thermoelectric thermopower.**
24. Waske, A. et al. Energy harvesting near room temperature using a thermomagnetic generator with a pretzel-like magnetic flux topology. *Nat. Energy* **4**, 68–74 (2019).
25. Liu, X. et al. High-performance thermomagnetic generator controlled by a magnetocaloric switch. *Nat. Commun.* **14**, 4811 (2023).
26. Tang, K. et al. Temperature-adaptive radiative coating for all-season household thermal regulation. *Science* **374**, 1504–1509 (2021). **This work shows the passive absorbance-emittance tunability via the nonlinear metal-insulator transition of  $W_2V_2O_{10}$  coatings around the ambient temperature.**
27. Wang, S. et al. Scalable thermochromic smart windows with passive radiative cooling regulation. *Science* **374**, 1501–1504 (2021).
28. Arena, S., Casti, E., Gasia, J., Cabeza, L. F. & Cau, G. Numerical simulation of a finned-tube LHTES system: influence of the mushy zone constant on the phase change behaviour. *Energy Procedia* **126**, 517–524 (2017).
29. Cattaneo, C. Sulla conduzione del calore. *Atti Sem. Mat. Fis. Univ. Modena* **3**, 83–101 (1948).
30. Joseph, D. D. & Preziosi, L. Heat waves. *Rev. Mod. Phys.* **61**, 41–73 (1989).
31. Guo, Y. & Wang, M. Phonon hydrodynamics and its applications in nanoscale heat transport. *Phys. Rep.* **595**, 1–44 (2015).
32. Callaway, J. Model for lattice thermal conductivity at low temperatures. *Phys. Rev.* **113**, 1046–1051 (1959).
33. Jiang, Y. et al. Evolution of defect structures leading to high ZT in GeTe-based thermoelectric materials. *Nat. Commun.* **13**, 6087 (2022).
34. Shen, M. et al. Thermoelectric coupling effect in BNT-BZT-xGaN pyroelectric ceramics for low-grade temperature-driven energy harvesting. *Nat. Commun.* **14**, 7907 (2023).
35. Byeon, D. et al. Discovery of colossal Seebeck effect in metallic  $Cu_2Se$ . *Nat. Commun.* **10**, 72 (2019).
36. Zhang, Z. et al.  $Cu_2Se$ -based liquid-like thermoelectric materials: looking back and stepping forward. *Energy Environ. Sci.* **13**, 3307–3329 (2020).
37. Li, H., Bowen, C. R. & Yang, Y. Phase transition enhanced pyroelectric nanogenerators for self-powered temperature sensors. *Nano Energy* **102**, 107657 (2022).
38. Li, T. et al. Thermoelectric properties and performance of flexible reduced graphene oxide films up to 3,000 K. *Nat. Energy* **3**, 148–156 (2018).
39. Fu, C. et al. Realizing high figure of merit in heavy-band p-type half-Heusler thermoelectric materials. *Nat. Commun.* **6**, 8144 (2015).
40. Ding, T. et al. Hybrid photothermal pyroelectric and thermogalvanic generator for multisituation low grade heat harvesting. *Adv. Energy Mater.* **8**, 1802397 (2018).
41. Lee, J. et al. Enhanced pyroelectric conversion of thermal radiation energy: energy harvesting and non-contact proximity sensor. *Nano Energy* **97**, 107178 (2022).
42. Gokana, M. R., Wu, C.-M., Matora, K. G., Qi, J. Y. & Yen, W.-T. Effects of patterned electrode on near infrared light-triggered cesium tungsten bronze/poly(vinylidene)fluoride nanocomposite-based pyroelectric nanogenerator for energy harvesting. *J. Power Sources* **536**, 231524 (2022).
43. Park, T. et al. Photothermally activated pyroelectric polymer films for harvesting of solar heat with a hybrid energy cell structure. *ACS Nano* **9**, 11830–11839 (2015).
44. Zhao, T. et al. An infrared-driven flexible pyroelectric generator for non-contact energy harvester. *Nanoscale* **8**, 8111–8117 (2016).
45. Ma, N., Zhang, K. & Yang, Y. Photovoltaic-pyroelectric coupled effect induced electricity for self-powered photodetector system. *Adv. Mater.* **29**, 1703694 (2017).
46. Song, K., Ma, N., Mishra, Y. K., Adelung, R. & Yang, Y. Achieving light-induced ultrahigh pyroelectric charge density toward self-powered UV light detection. *Adv. Electron. Mater.* **5**, 1800413 (2019).
47. Jurado, J. P. et al. Solar harvesting: a unique opportunity for organic thermoelectrics? *Adv. Energy Mater.* **9**, 1902385 (2019).
48. Li, K. et al. Enhanced thermoelectric performance and tunable polarity in 2D  $Cu_2S$ -phenol superlattices composites for solar energy conversion. *Nano Energy* **84**, 105902 (2021).
49. Cho, C., Kim, B., Park, S. & Kim, E. Bisulfate transport in hydrogels for self-healable and transparent thermoelectric harvesting films. *Energy Environ. Sci.* **15**, 2049–2060 (2022).
50. Wei, M. et al. Directional thermal diffusion realizing inorganic  $Sb_2Te_3$ /Te hybrid thin films with high thermoelectric performance and flexibility. *Adv. Funct. Mater.* **32**, 2207903 (2022).
51. Chen, C. et al. Janus helical ribbon structure of ordered nanowire films for flexible solar thermoelectric devices. *Adv. Mater.* **34**, 2206364 (2022).
52. Lu, Y. et al. Staggered-layer-boosted flexible  $Bi_2Te_3$  films with high thermoelectric performance. *Nat. Nanotechnol.* **18**, 1281–1288 (2023). **This work realizes high thermoelectricity and flexibility in mechanically exfoliated thin films alongside spatial in-plane thermal regulation via atomic and macroscale topology manipulations.**
53. Zhu, L., Gao, M., Peh, C. K. N., Wang, X. & Ho, G. W. Self-contained monolithic carbon sponges for solar-driven interfacial water evaporation distillation and electricity generation. *Adv. Energy Mater.* **8**, 1702149 (2018).
54. Meng, F. L. et al. Modular and deformable steam electricity co-generation system with photothermal, water and electrochemical tunable multilayers. *Adv. Funct. Mater.* **30**, 2002867 (2020).
55. Yang, M.-Q., Tan, C. F., Lu, W., Zeng, K. & Ho, G. W. Spectrum tailored defective 2D semiconductor nanosheets aerogel for full-spectrum-driven photothermal water evaporation and photochemical degradation. *Adv. Funct. Mater.* **30**, 2004460 (2020).
56. Qian, X., Zhou, J. & Chen, G. Phonon-engineered extreme thermal conductivity materials. *Nat. Mater.* **20**, 1188–1202 (2021).
57. Born, M. On the quantum theory of pyroelectricity. *Rev. Mod. Phys.* **17**, 245–251 (1945).
58. Mankowsky, R., von Hoegen, A., Forst, M. & Cavalleri, A. Ultrafast reversal of the ferroelectric polarization. *Phys. Rev. Lett.* **118**, 197601 (2017).
59. Henstridge, M., Först, M., Rowe, E., Fechner, M. & Cavalleri, A. Nonlocal nonlinear phononics. *Nat. Phys.* **18**, 457–461 (2022).
60. Meirzadeh, E. et al. Surface pyroelectricity in cubic  $SrTiO_3$ . *Adv. Mater.* **31**, 1904733 (2019).
61. Jiang, Y. et al. Direct atom-by-atom chemical identification of nanostructures and defects of topological insulators. *Nano Lett.* **13**, 2851–2856 (2013).
62. Huang, X. et al. Stacking fault-induced strengthening mechanism in thermoelectric semiconductor  $Bi_2Te_3$ . *Matter* **6**, 3087–3098 (2023).
63. Zhou, Y. et al. Physics-guided co-designing flexible thermoelectrics with techno-economic sustainability for low-grade heat harvesting. *Sci. Adv.* **9**, eadf5701 (2023). **This work unravels the quasi-linear coupling characteristics between conductive heat flux and electrical power in non-unity geometric thermoelectrics.**
64. Zhou, Y. et al. Controlled heterogeneous water distribution and evaporation towards enhanced photothermal water-electricity-hydrogen production. *Nano Energy* **77**, 105102 (2020).
65. Mori, T. A flexible feature for the long-reigning thermoelectric champion bismuth telluride. *Nat. Nanotechnol.* **18**, 1255–1256 (2023).
66. Kang, M. G. & Guo, L. J. Nanoimprinted semitransparent metal electrodes and their application in organic light-emitting diodes. *Adv. Mater.* **19**, 1391–1396 (2007).
67. Lee, H. B., Jin, W.-Y., Ovhal, M. M., Kumar, N. & Kang, J.-W. Flexible transparent conducting electrodes based on metal meshes for organic optoelectronic device applications: a review. *J. Mater. Chem. C* **7**, 1087–1110 (2019).
68. Zabeck, D., Taylor, J., Boulbar, E. L. & Bowen, C. R. Micropatterning of flexible and free standing polyvinylidene difluoride (PVDF) films for enhanced pyroelectric energy transformation. *Adv. Energy Mater.* **5**, 1401891 (2015).
69. Stewart, J. W., Vella, J. H., Li, W., Fan, S. & Mikkelsen, M. H. Ultrafast pyroelectric photodetection with on-chip spectral filters. *Nat. Mater.* **19**, 158–162 (2020).
70. Padilla, W. J. & Averitt, R. D. Imaging with metamaterials. *Nat. Rev. Phys.* **4**, 85–100 (2022).
71. Stewart, J. W., Nebabu, T. & Mikkelsen, M. H. Control of nanoscale heat generation with lithography-free metasurface absorbers. *Nano Lett.* **22**, 5151–5157 (2022).
72. Yang, Y. et al. Pyroelectric nanogenerators for harvesting thermoelectric energy. *Nano Lett.* **12**, 2833–2838 (2012).
73. Jiang, J. et al. Giant pyroelectricity in nanomembranes. *Nature* **607**, 480–485 (2022).
74. Liu, J. & Pantelides, S. T. Mechanisms of pyroelectricity in three- and two-dimensional materials. *Phys. Rev. Lett.* **120**, 207602 (2018). **This work reveals the dominant factor of rigid-ion model and/or electron-phonon renormalization in boosting the pyroelectricity of 3D and 2D pyroelectric materials.**
75. Lheritier, P. et al. Large harvested energy with non-linear pyroelectric modules. *Nature* **609**, 718–721 (2022). **This work realizes nonlinear pyroelectric heat harvesting via the applied thermal field (entropy-temperature plane) and applied electric field (polarization-electric field plane) alongside multilayered capacitors around the ambient or Curie temperature.**
76. Olsen, R. B., Bruno, D. A. & Briscoe, J. M. Pyroelectric conversion cycles. *J. Appl. Phys.* **58**, 4709–4716 (1985).
77. Ng, M. H. V. et al. in *Comprehensive Energy Systems* Vol. 2 (ed. Dincer, I.) Ch. 2.23, 720–759 (Elsevier, 2018).
78. Kim, J. et al. High-performance piezoelectric, pyroelectric, and triboelectric nanogenerators based on P(VDF-TrFE) with controlled crystallinity and dipole alignment. *Adv. Funct. Mater.* **27**, 1700702 (2017).
79. Navid, A., Lynch, C. S. & Pilon, L. Purified and porous poly(vinylidene fluoride-trifluoroethylene) thin films for pyroelectric infrared sensing and energy harvesting. *Smart Mater. Struct.* **19**, 055006 (2010).
80. Wang, Q. et al. Hexagonal boron nitride nanosheets doped pyroelectric ceramic composite for high-performance thermal energy harvesting. *Nano Energy* **60**, 144–152 (2019).
81. Yan, M. et al. Porous ferroelectric materials for energy technologies: current status and future perspectives. *Energy Environ. Sci.* **14**, 6158–6190 (2021).
82. Feng, J. et al. Porous thermoelectric Zintl:  $YbCd_2Sb_2$ . *ACS Appl. Energy Mater.* **4**, 913–920 (2021).

83. Zhang, C., Zeng, Z., Zhu, Z., Karami, M. & Chen, X. Impact of leakage for electricity generation by pyroelectric converter. *Phys. Rev. Appl.* **14**, 064079 (2020).
84. Zhou, Y. et al. Non-planar dielectrics derived thermal and electrostatic field inhomogeneity for boosted weather-adaptive energy harvesting. *Nat. Sci. Rev.* **10**, nwad186 (2023).
85. Zhou, Y. & Ho, G. W. Pyroelectric heat harvesting, what's next. *Next Energy* **1**, 100026 (2023).
86. Yang, S. Y. et al. Above-bandgap voltages from ferroelectric photovoltaic devices. *Nat. Nanotechnol.* **5**, 143–147 (2010).
87. Spanier, J. E. et al. Power conversion efficiency exceeding the Shockley–Queisser limit in a ferroelectric insulator. *Nat. Photon.* **10**, 611–616 (2016).
88. Ni, G. et al. Steam generation under one sun enabled by a floating structure with thermal concentration. *Nat. Energy* **1**, 16126 (2016).
- This work utilizes the synergistic effect of spatial thermal concentration and vapour diffusion to achieve a high solar water evaporation efficiency.**
89. Gao, T. et al. More from less: improving solar steam generation by selectively removing a portion of evaporation surface. *Sci. Bull.* **67**, 1572–1580 (2022).
90. Zhang, L. et al. Passive, high-efficiency thermally-localized solar desalination. *Energy Environ. Sci.* **14**, 1771–1793 (2021).
91. Zhou, Y. et al. Dynamic piezo-thermoelectric generator for simultaneously harvesting mechanical and thermal energies. *Nano Energy* **69**, 104397 (2020).
92. Choo, S. et al. Geometric design of Cu<sub>2</sub>Se-based thermoelectric materials for enhancing power generation. *Nat. Energy* **9**, 1105–1116 (2024).
93. Allen, P. B. & Heine, V. Theory of the temperature dependence of electronic band structures. *J. Phys. C Solid State Phys.* **9**, 2305 (1976).
94. Born, M. & Huang, K. in *Dynamical Theory of Crystal Lattices* Vol. 1 Ch. 6, 287–288 (Oxford Univ. Press, 1954).
95. Li, H., Bowen, C. R., Dan, H. & Yang, Y. Pyroelectricity induced by Schottky interface above the Curie temperature of bulk materials. *Joule* **8**, 401–415 (2024).
96. Yang, L. et al. Suppressed thermal transport in silicon nanoribbons by inhomogeneous strain. *Nature* **629**, 1021–1026 (2024).
97. Fatuzzo, E., Kiess, H. & Nitsche, R. Theoretical efficiency of pyroelectric power converters. *J. Appl. Phys.* **37**, 510–516 (1966).
98. Goldsmid, H. J. & Sharp, J. W. Estimation of the thermal band gap of a semiconductor from Seebeck measurements. *J. Electron. Mater.* **28**, 869–872 (1999).
99. Snyder, G. J. & Toberer, E. S. Complex thermoelectric materials. *Nat. Mater.* **7**, 105–114 (2008).
100. Han, S. et al. Strong phonon softening and avoided crossing in aliovalence-doped heavy-band thermoelectrics. *Nat. Phys.* **19**, 1649–1657 (2023).
101. Uchida, K.-I & Heremans, J. P. Thermoelectrics: from longitudinal to transverse. *Joule* **6**, 2240–2245 (2022).
102. Yang, G. et al. The role of spin in thermoelectricity. *Nat. Rev. Phys.* **5**, 466–482 (2023).
103. Zhu, H. et al. Understanding the asymmetrical thermoelectric performance for discovering promising thermoelectric materials. *Sci. Adv.* **5**, eaav5813 (2019).
104. Ivry, Y. et al. Enhanced pyroelectric effect in self-supported films of BaTiO<sub>3</sub> with polycrystalline macrodomains. *Appl. Phys. Lett.* **90**, 172905 (2007).
105. Xu, L. et al. Free-form and multi-physical metamaterials with forward conformality-assisted tracing. *Nat. Comput. Sci.* **4**, 532–541 (2024).
106. Merchant, A. et al. Scaling deep learning for materials discovery. *Nature* **624**, 80–85 (2023).
107. Szymanski, N. J. et al. An autonomous laboratory for the accelerated synthesis of novel materials. *Nature* **624**, 86–91 (2023).
108. Biswas, K. et al. High-performance bulk thermoelectrics with all-scale hierarchical architectures. *Nature* **489**, 414–418 (2012).
109. Jiang, B. et al. High-entropy-stabilized chalcogenides with high thermoelectric performance. *Science* **371**, 830–834 (2021).
110. Zhou, Y., Guo, Z. & He, J. Redesign high-performance flexible thermoelectrics: from mathematical algorithm to artificial cracks. *Appl. Phys. Lett.* **116**, 043904 (2020).
111. Xie, L. et al. Screening strategy for developing thermoelectric interface materials. *Science* **382**, 921–928 (2023).
112. Lara Ramos, D. A. et al. Design guidelines for micro-thermoelectric devices by finite element analysis. *Adv. Sustain. Syst.* **3**, 1800093 (2019).
113. Gorai, P., Stevanović, V. & Toberer, E. S. Computationally guided discovery of thermoelectric materials. *Nat. Rev. Mater.* **2**, 17053 (2017).
114. Wang, T., Zhang, C., Snoussi, H. & Zhang, G. Machine learning approaches for thermoelectric materials research. *Adv. Funct. Mater.* **30**, 1906041 (2019).
115. Gaultois, M. W. et al. Data-driven review of thermoelectric materials: performance and resource considerations. *Chem. Mater.* **25**, 2911–2920 (2013).
116. Yin, L. et al. CALPHAD accelerated design of advanced full-Zintl thermoelectric device. *Nat. Commun.* **15**, 1468 (2024).
117. Bastek, J.-H. & Kochmann, D. M. Inverse design of nonlinear mechanical metamaterials via video denoising diffusion models. *Nat. Mach. Intell.* **5**, 1466–1475 (2023).
118. Luo, S. et al. Experiment-free exoskeleton assistance via learning in simulation. *Nature* **630**, 353–359 (2024).
119. APRE CDTI. *Guiding Notes to Use the TRL Self-Assessment Tool*. Report No. H2020-101005071 (BRIDGE2HE, 2020).
120. US Department of Energy. *Technology Readiness Assessment Guide*. Report No. DOE G 413.3-4A (US Department of Energy, 2011).
121. US Government Accountability Office. *Technology Readiness Assessment Guide: Best Practices for Evaluating the Readiness of Technology for Use in Acquisition Programs and Projects*. Report No. GAO-20-48G (US Government Accountability Office, 2020).
122. Xu, G. et al. Tunable analog thermal material. *Nat. Commun.* **11**, 6028 (2020).
123. Guo, J., Xu, G., Tian, D., Qu, Z. & Qiu, C. W. Passive ultra-conductive thermal metamaterials. *Adv. Mater.* **34**, 2200329 (2022).
124. Li, Y. et al. Transforming heat transfer with thermal metamaterials and devices. *Nat. Rev. Mater.* **6**, 488–507 (2021).
125. Karthikeyan, V. et al. Three dimensional architected thermoelectric devices with high toughness and power conversion efficiency. *Nat. Commun.* **14**, 2069 (2023).
126. Xu, L. et al. Blackhole-inspired thermal trapping with graded heat-conduction metadevices. *Nat. Sci. Rev.* **10**, nwad159 (2022).
127. Jiao, P., Mueller, J., Raney, J. R., Zheng, X. & Alavi, A. H. Mechanical metamaterials and beyond. *Nat. Commun.* **14**, 6004 (2023).
128. Kai, Y. et al. Dynamic diagnosis of metamaterials through laser-induced vibrational signatures. *Nature* **623**, 514–521 (2023).
129. Ren, W. et al. High-performance wearable thermoelectric generator with self-healing, recycling, and Lego-like reconfiguring capabilities. *Sci. Adv.* **7**, eabe0586 (2021).
130. Yang, Q. et al. Flexible thermoelectrics based on ductile semiconductors. *Science* **377**, 854–858 (2022).
131. Ding, T. et al. Scalable thermoelectric fibers for multifunctional textile-electronics. *Nat. Commun.* **11**, 6006 (2020).
132. Yu, C. & Chau, K. T. Thermoelectric automotive waste heat energy recovery using maximum power point tracking. *Energy Convers. Manag.* **50**, 1506–1512 (2009).
133. Meng, J.-H., Wang, X.-D. & Chen, W.-H. Performance investigation and design optimization of a thermoelectric generator applied in automobile exhaust waste heat recovery. *Energy Convers. Manag.* **120**, 71–80 (2016).
134. LeBlanc, S., Yee, S. K., Scullin, M. L., Dames, C. & Goodson, K. E. Material and manufacturing cost considerations for thermoelectrics. *Renew. Sustain. Energy Rev.* **32**, 313–327 (2014).
135. Amatya, R. & Ram, R. J. Trend for thermoelectric materials and their earth abundance. *J. Electron. Mater.* **41**, 1011–1019 (2011).
136. Yee, S. K., LeBlanc, S., Goodson, K. E. & Dames, C. \$ per W metrics for thermoelectric power generation: beyond ZT. *Energy Environ. Sci.* **6**, 2561–2571 (2013).
137. Lee, W. H. *A Pressure Iteration Scheme for Two-Phase Flow Modeling*. Report No. 978-981-4460-27-9 (World Scientific, 2013).
138. Gong, F. et al. Sustainable, decentralized water treatment system fabricated from domestic waste materials and ultrafast-reduced graphene oxide. *J. Environ. Chem. Eng.* **11**, 110480 (2023).
139. Jachalke, S. et al. How to measure the pyroelectric coefficient? *Appl. Phys. Rev.* **4**, 021303 (2017).
140. Salazar, P. F., Kumar, S. & Cola, B. A. Design and optimization of thermo-electrochemical cells. *J. Appl. Electrochem.* **44**, 325–336 (2014).
141. Kishore, R. A. et al. Linear thermomagnetic energy harvester for low-grade thermal energy harvesting. *J. Appl. Phys.* **127**, 044501 (2020).
142. Yang, S. E. et al. Composition-segmented BiSbTe thermoelectric generator fabricated by multimaterial 3D printing. *Nano Energy* **81**, 105638 (2021).
143. Kim, K. et al. Heat-dissipation design and 3D printing of ternary silver chalcogenide-based thermoelectric legs for enhancing power generation performance. *Adv. Sci.* **11**, e2402934 (2024).
144. New York State Energy Research and Development Authority. Technology & commercialization readiness level calculator. <https://portal.nyseda.ny.gov/servlet/servlet.FileDownload?file=00P00000012HX3EAN> (2015).
145. United Nations. Resolution adopted by the general assembly on 6 July 2017: work of the statistical commission pertaining to the 2030 Agenda for Sustainable Development. *United Nations* [https://ggim.un.org/documents/a\\_res\\_71\\_313.pdf](https://ggim.un.org/documents/a_res_71_313.pdf) (2017).
146. Zhao, L. et al. A passive high-temperature high-pressure solar steam generator for medical sterilization. *Joule* **4**, 2733–2745 (2020).
147. Li, J. et al. Printable, emissivity-adaptive and albedo-optimized covering for year-round energy saving. *Joule* **7**, 2552–2567 (2023).
148. Zhang, Z. et al. Diffusion metamaterials. *Nat. Rev. Phys.* **5**, 218–235 (2023).
149. Yang, S., Liu, M., Zhao, C., Fan, S. & Qiu, C.-W. Nonreciprocal thermal photonics. *Nat. Photon.* **18**, 412–424 (2024).
150. Zhang, Z. & Zhu, L. Nonreciprocal thermal photonics for energy conversion and radiative heat transfer. *Phys. Rev. Appl.* **18**, 027001 (2022).
151. Nam Sung, K., Flautner, K., Blaauw, D. & Mudge, T. Circuit and microarchitectural techniques for reducing cache leakage power. *IEEE Trans. Very Large Scale Integr. VLSI Syst.* **12**, 167–184 (2004).
152. Wu, C.-J. Architectural thermal energy harvesting opportunities for sustainable computing. *IEEE Comput. Archit. Lett.* **13**, 65–68 (2014).
153. McCord, P. Plot of altitude vs temperature. *Chembook* <http://chembook.org/page-nonav.php?chnum=2&sect=3> (2019).

## Acknowledgements

This research was supported by A\*STAR, RIE2025 Manufacturing, Trade and Connectivity (MTC) (M22K2c0081), the Advanced Research and Technology Innovation Centre (ARTIC) and the National University of Singapore (A-0005947-24-00). J.H. acknowledges support from the National Natural Science Foundation of China (11934007) and the Outstanding Talents Training Fund in Shenzhen (202108). T.D. acknowledges support from the National Natural Science Foundation of China (52472088). C.-W.Q. acknowledges support from Ministry of Education, Singapore (A-8000107-01-00) and the Nanotech Energy and Environment Platform, National University of Singapore (Suzhou) Research Institute via Science and

Technology Project of Jiangsu Province (BZ2022056). This research is also partially supported by the National Research Foundation, Singapore (NRF) under NRF's Medium Sized Centre: Singapore Hybrid-Integrated Next-Generation  $\mu$ -Electronics (SHINE) Centre funding programme.

## Author contributions

Y.Z. and G.W.H. conceptualized the manuscript. C.-W.Q., J.H. and G.W.H. supervised the project. Y.Z., T.D., G.X. and S.Y. researched data for the article. Y.Z. and T.D. conceived and illustrated the figures and tables. Y.Z. wrote the paper with input and comments from all authors. All authors contributed to the discussion and editing of the content of the manuscript before submission.

## Competing interests

The authors declare no competing interests.

## Additional information

**Peer review information** *Nature Reviews Physics* thanks Chris Bowen, Weishu Liu and Qi Zhao for their contributions to the peer review of this work.

**Publisher's note** Springer Nature remains neutral with regard to jurisdictional claims in published maps and institutional affiliations.

Springer Nature or its licensor (e.g. a society or other partner) holds exclusive rights to this article under a publishing agreement with the author(s) or other rightsholder(s); author self-archiving of the accepted manuscript version of this article is solely governed by the terms of such publishing agreement and applicable law.

© Springer Nature Limited 2024